remote sensing

MDPI

Article

Climate Interprets Saturation Value Variations Better Than Soil and Topography in Estimating Oak Forest Aboveground Biomass Using Landsat 8 OLI Imagery

Yong Wu [1,2], Guanglong Ou [1,2,*], Tianbao Huang [1,2], Xiaoli Zhang [1,2], Chunxiao Liu [1,2], Zhi Liu [1,2], Zhibo Yu [1,2], Hongbin Luo [1,2], Chi Lu [1,2], Kaize Shi [3], Leiguang Wang [1,4] and Weiheng Xu [1,4]

[1] Key Laboratory of State Administration of Forestry and Grassland on Biodiversity Conservation in Southwest China, Southwest Forestry University, Kunming 650233, China; yongwu@swfu.edu.cn (Y.W.); huangtianbao@swfu.edu.cn (T.H.); karojan@swfu.edu.cn (X.Z.); liuchunxiao@swfu.edu.cn (C.L.); liuzhi@swfu.edu.cn (Z.L.); yuzhibo@swfu.edu.cn (Z.Y.); luohongbin@swfu.edu.cn (H.L.); luchi666666@swfu.edu.cn (C.L.); leiguangwang@swfu.edu.cn (L.W.); xwh@swfu.edu.cn (W.X.)
[2] Key Laboratory for Forest Resources Conservation and Utilization in the Southwest Mountains of China, Ministry of Education, Southwest Forestry University, Kunming 650233, China
[3] Yunnan Institute of Forest Inventory and Planning, Kunming 650051, China; niejing@swfu.edu.cn
[4] Institute of Big Data and Artificial Intelligence, Southwest Forestry University, Kunming 650224, China
* Correspondence: olg2007621@swfu.edu.cn

Abstract: The optical saturation problem is one of the main factors causing uncertainty in aboveground biomass (AGB) estimations using optical remote sensing data. It is critical for the improvement in AGB estimation accuracy to clarify the relationships between environmental factors and the variations in optical saturation values (OSVs). In this study, we obtained the OSVs for 20 districts and clarified the individual, interactive, and comprehensive effects of climate, soil, and topographical factors on the OSV variations. The results are as follows: (1) the range of the OSVs was from 104 t/hm^2 to 182 t/hm^2 for the 20 districts; (2) the soil factor had the greatest (−0.635) influence on the OSVs compared to climate and topography; (3) the highest interaction effect (−0.833) was between climate and soil; (4) the comprehensive effect of the three environmental factors on the OSVs was obvious, and the correlation coefficient was 0.436. Moreover, the mean temperature of the coldest quarter (MCQMean) had the highest effect on the OSVs. The results indicate that environmental factors significantly affect the variation in OSVs through their individual, interactive, and comprehensive effects. Our findings provide a valuable reference for reducing the uncertainty caused by spectral saturation in AGB estimations using optical remote sensing data.

Keywords: optical saturation values variation; climate factors; topography factors; soil factors; oak forests; Landsat 8 OLI imagery

Citation: Wu, Y.; Ou, G.; Huang, T.; Zhang, X.; Liu, C.; Liu, Z.; Yu, Z.; Luo, H.; Lu, C.; Shi, K.; et al. Climate Interprets Saturation Value Variations Better Than Soil and Topography in Estimating Oak Forest Aboveground Biomass Using Landsat 8 OLI Imagery. *Remote Sens.* **2024**, *16*, 1338. https://doi.org/10.3390/rs16081338

Academic Editors: Gherardo Chirici, Alessio Collalti and Elia Vangi

Received: 5 March 2024
Revised: 5 April 2024
Accepted: 8 April 2024
Published: 10 April 2024

1. Introduction

Forest biomass plays a vital role in the forest ecosystem, and it is the foundation of forest carbon dynamics and carbon cycle analyses [1]. Thus, its accurate estimation becomes very important and is of wide concern [2]. Most studies on forest aboveground biomass (AGB) have focused on field surveys prior to the introduction of efficient technology such as remote sensing [3]. Nowadays, remotely sensed data are widely used in the mapping, estimating, and monitoring of biomass on a large scale [4]. Many different sensor data, including radar, optical, and LiDAR, are available for AGB estimation, and integrated data sources have higher accuracy [5]. But significant challenges have been recognized concerning improving the accuracy of estimations and reducing the uncertainties of AGB remote sensing estimations, especially with optical remote sensing estimation, and numerous studies have been conducted to investigate the causes of uncertainty and methods for improving accuracy [6,7].

Although radar and LiDAR have a higher correlation with forest AGB [8], they are limited by their high costs and complex data processing, especially on a large scale [8,9]. Conversely, optical remote sensing imagery stands out for its widespread availability, lower cost, and established processing techniques, offering distinct advantages in large-scale monitoring [10], especially the wall-to-wall availability and frequent temporal resolution of most satellite missions for optical remote sensing data [11]. Optical images (e.g., Landsat MODIS/TM/ETM+/OLI and Sentinel-2 images) are widely used in AGB estimation due to the high relationship between the spectral variables and AGB [12]. The high-resolution optical imagery also provided by satellites, like Landsat 8 and Sentinel-2A, allows for detailed analysis of vegetation cover, structure, and even species composition, which are critical factors in estimating AGB [7,13,14]. Specifically, Huang et al. [15] underscored the critical role of Landsat 8 and Sentinel-2A optical imagery in accurately estimating AGB in Yunnan's mixed forests. Imran and Ahmed [16], alongside Li et al. [17], showcased the capabilities of Landsat 8 imagery in accurately assessing forest AGB and carbon storage, which is part of a growing body of evidence that highlights the indispensable role of optical remote sensing technology in forest management research [2,18].

Unfortunately, spectral reflectance values lose their sensitivity to increases in AGB upon reaching a certain threshold, which causes the common optical saturation problem in most relevant studies, especially in densely vegetated regions and higher heterogeneous forest areas [19,20]. Moreover, the saturation of optical remote sensing data is one of the main factors that result in uncertainty [21], and it easily causes underestimation of larger biomass values due to the complex forest environment, high forest density, and heterogeneity [2,22]. To overcome the optical saturation problem, many studies have investigated the relationships between AGB and remote sensing variables among various vegetation types and regions by incorporating multisource data (such as optical and radar) and/or using machine learning and deep learning methods to improve the accuracy of AGB estimations [23]. For instance, Steininger [24] correlated band reflectance with biomass and showed that the near-infrared band (NIR) of Landsat TM imagery tends to decrease linearly with an increasing stand age and biomass. Zhu and Liu [25] achieved a more accurate AGB estimation and less saturation using a seasonal NDVI time series than a single NDVI with Landsat data. Chen et al. [26] leveraged Sentinel-2 remote sensing data to assess a bamboo forest's AGB in Zhejiang, China, revealing that optical sensor data face saturation challenges in accurately modeling AGB. Jha et al. [27] evaluated the efficacy of Landsat-8, Sentinel-2B, and Worldview-3 satellite sensors in the mapping forest of AGB in Thailand, revealing varying performances and saturation points among sensors. Meanwhile, Zhao et al. [20] utilized the SWIR2 band of Landsat TM data to estimate AGB, and the results showed that the spherical model had smaller residuals and higher accuracy in subtropical regions in obtaining the OSVs, as well as indicating that the different vegetation types had various OSVs. In summary, they found that the optical saturation problem was the key factor in the uncertainty in forest AGB estimations, especially underestimation, which caused a larger error in forest AGB estimations. Although many studies have achieved a high estimation accuracy, the saturation problem still exists. Therefore, it is of great significance to explore the variations in and distribution patterns of optical saturation and identify the main factors influencing forest AGB estimations using optical remote sensing data.

Generally, OSVs vary among different forest types, study areas, and optical remote sensing sources [19,28,29]. The variations in and distributions of OSVs may be affected by environmental factors, such as climate, topography, and soil [30], because environmental heterogeneity may result in variations in the forest types and stand structures. Climate is an important factor that causes different forest heterogeneities, forest types, species compositions, and forest distributions [31]. For instance, the annual ranges of temperature variation during the coldest season, climate heterogeneity, and precipitation were all main factors that caused the variation in forests [32]. The soil heterogeneity affects the competitive ability of different species, which is one reason for the forest types and stand structure diversity [33]. Additionally, the topography is also one of the main factors

affecting the distribution of vegetation types and forest AGB [34]. For instance, slope, aspect, and altitude are all influential factors affecting the distribution of vegetation types, as shady slopes receive less sunlight, resulting in cooler and moister conditions, while sunny slopes tend to be warmer and drier [35]. Altitude is a crucial variable since it affects temperature, precipitation, and atmospheric pressure, which results in differences in species distribution [36]. So, climate, topography, and soil factors are the main factors that affect the distributions of forest types and species, which lead to various spectral reflectance thresholds, resulting in different optical saturation values. Herein, the key environmental factors, or variables, affecting OSV variation are explored, which have rarely been reported.

Overall, this study establishes a foundational framework for investigating the variability in and distribution patterns of optical saturation, discerning the primary environmental determinants influencing OSVs. This, in turn, aims to address the challenge of optical saturation and to elevate the precision of AGB estimations using optical remote sensing data. Yunnan province—known as the Kingdom of Plants—located in southwestern China, is a region with high forest heterogeneity [37], and oak forests are one of its most widespread and significant vegetation types. So, we selected oak forests in the different vegetation regions in Yunnan province as the research objects. Then, we obtained the OSVs for the AGB estimations by the spherical model using Landsat 8 OLI images and analyzed the relationships between the OSVs and climate, topographic, and soil variables to clarify the environmental effects on the variation in the OSVs. The objectives of this study were as follows:

1. Clarify the relationships between the OSVs and climate, topographic, and soil variables.
2. Identify the key environmental variables that determine the variations in the OSVs.
3. Explore the interactive and comprehensive effect of the three types of environmental factors on the variation in the OSVs.

2. Materials and Methods

The methodological framework of this study, as shown in Figure 1, comprised the following steps: (1) collecting data on oak forest AGBs and sample plots; (2) calculating the oak forest AGBs; (3) acquiring, processing, and analyzing the Landsat 8 OLI images and DEMs; (4) selecting 20 districts in Yunnan province on the basis of Yunnan Vegetation; (5) obtaining the OSVs; (6) comparing the OSVs among the 20 districts; (7) interpreting the environmental factors that affect the variability in the OSVs; and (8) identifying the primary environmental factors that impact the OSVs.

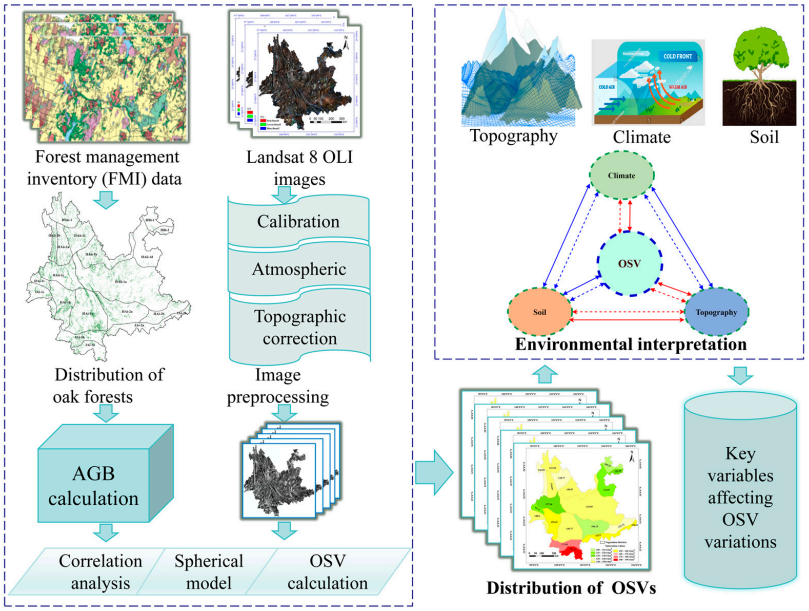

Figure 1. Flow chart of the methodology used in this study to estimate the OSVs and analyze the variations.

2.1. Study Area and Objects

Yunnan province, southwest China, is located between 97°31′–106°11′E and 21°8′–29°15′N. The area reaches 394,000 km^2, and the Tropic of Cancer crosses the southern part of the province (Figure 2). It is higher in elevation in the northwest and lower in the southeast, with a stepwise decline from the northwest to southeast. It is predominantly composed of mountains and highlands, with altitudes in the range from 76.4 to 6740 m [38]. Moreover, it covers cold, warm, and tropical zones, and the highest average monthly temperature is from 19 °C to 22 °C, while the coldest month experiences an average temperature between 6 °C and 8 °C [39]. The annual temperature ranges from 10 °C to 12 °C, and the precipitation ranges from 500 mm to 2700 mm, which generates extremely abundant vegetation types [15]. Oak forests are pioneers in barren wasteland and afforested areas, with strong adaptability and carbon sequestration capacities, making it one of the most widespread and significant vegetation types in Yunnan province. According to the eighth national forest resources continuous inventory of China, the total natural oak forest area is 1.91 million hectares in Yunnan province, which accounts for 10.28% of the total forest area in Yunnan. Moreover, natural oak forests in Yunnan have a total storage volume of 239.36 million m^3, which accounts for 12.1% of the total forest storage volume in Yunnan. Thus, they play an important role in ensuring wood safety and a stable ecological environment [40,41]. In Yunnan, the main oak forests comprise evergreen trees, and the dominant tree species include *Castanopsis fargesii*, *Castanopsis hystrix*, *Cyclobalanopsis glauca*, *Quercus semicarpifolia*, *Lithocarpus xylocarpus*, *Castanopsis delavayi*, and *Lithocarpus microsperma* [39,42].

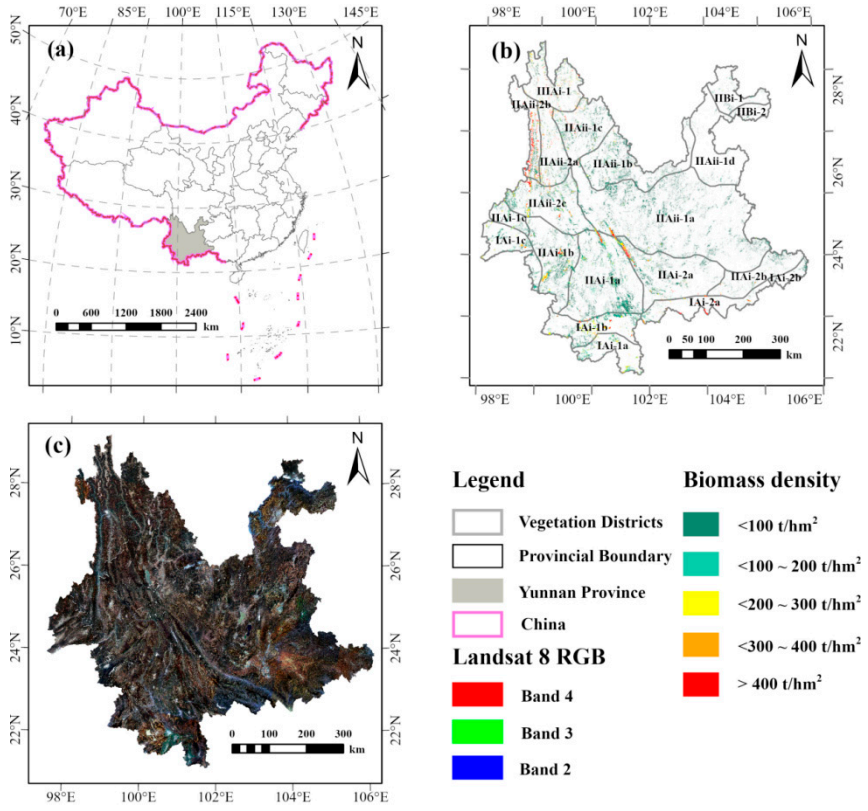

Figure 2. Maps of the study area: (**a**) location of Yunnan province in China; (**b**) distribution of oak forests and the 20 districts in Yunnan province; (**c**) Landsat 8 OLI image from 2016 of Yunnan province.

2.2. Vegetation Districts in Yunnan Province

According to the vegetation regionalization map in Yunnan Vegetation, there are 4 regions, 4 subregions, 5 zones, 3 districts, and 17 subdistricts in Yunnan province [39]. We chose subdistricts as the basic unit of zoning for this study. Because of the smaller areas of three districts, they are not divided into subdistricts; 17 subdistricts and 3 districts with

smaller areas were identified for a total of 20 "vegetation districts" in this study (Table 1). Moreover, we digitalized the district boundaries of the vegetation regionalization map to obtain the vector layers using ArcGIS 10.8 software (Figure 2).

Table 1. Vegetation districts of Yunnan province.

Regions	Subregions	Zones	Districts or Subdistricts
Region of tropical monsoon rainforests and tropical rainforests	Subregion of western (xerophytic) tropical rain forests and monsoon forests	Zone of seasonal rainforests and semi-evergreen seasonal rainforests at the northern margin of the monsoon tropics	Subdistrict of Antiaris toxicaria, Pouteria grandifolia, Canarium subulatum, Ficus altissima, and Chukrasia tabularis forests of the southern midmountain basin of Xishuangbanna (IAi-1a)
			Subdistrict of *Terminalia myriocarpa* and *Pometia pinnata* forests, *semecarpus albescens,* and *Machilus nanmu* forests of the northern midmountain basin of Xishuangbanna (IAi-1b)
			Subdistrict of *Ficus altissima* and *Chukrasia tabularis* forests of the middle and broad valleys of southwest Yunnan (IAi-1c)
			Subdistrict of *Dipterocarpus retusus, Hopea chinensis, Cinnamomum camphora, Camellia sinensis,* and *Magnolia* sp., forests of the Honghe and Wenshan Prefectures, south rim valley (IAi-2a)
			Subdistrict of *Lysidce rhodostegia* and *Ficus altissima* forests of the low mountain valleys of southeastern Wenshan Prefecture (IAi-2b)
Region of subtropical evergreen broad-leaved forests	Subregion of western (semi-humid) evergreen broad-leaved forests	Zone of subtropical monsoon evergreen broad-leaved forests of the southern plateau	Subdistrict of *Castanopsis hystrix, Castanopsis orthacantha*, and *Pinus yunnanensis* forests of the midmountain plateau, located in the middle reaches of the Lancang River (IIAi-1a)
			Subdistrict of *Castanopsis hystrix, Castanopsis indica,* and *Lithocarpuse chinotholus* forests of the mountains in Lincang (IIAi-1b)
			Subdistrict of *Castanopsis ferox*, *Castanopsis hystrix,* and *Lithocarpus truncatus* forests of the midmountainous plateaus of Longling and Lianghe (IIAi-1c)
			Subdistrict of *Pinus yunnanensis* and *Schima wallichii* forests and *Bombax ceiba* and *Woodfordia fruticosa* bushes of the karst plateau valley of Mengzi and Yuanjiang (IIAi-2a)
			Subdistrict of *Castanopsis faberi* and *Castanopsis fissa* forests of the Wenshan karst plateau (IIAi-2b)
		Zone of subtropical northern broad-leaved evergreen forests of the plateau	Subdistrict of *Quercus glaucoides, Castanopsis orthacantha*, and *Pinus yunnanensis* forests of the basin valley of the central Yunnan plateau (IIAii-1a)
			Subdistrict of *Pinus yunnanensis* and alpine oak forests in the middle and northern Yunnan mountain valleys (IIAii-1b)
			Subdistrict of *Pinus yunnanensis*, *Picea asperata*, and *Abies fabri* forests of the high mountain plateau of northwestern central Yunnan (IIAii-1c)
			Subdistrict of *Leymus chinensis* meadows and *Pinus yunnanensis* forest in the high and middle areas of the northeastern Yunnan plateau (IIAii-1d)
			Subdistrict of *Pinus yunnanensis*, *Castanopsis orthacantha*, and *Abies fabri* forests in the high and middle mountain valleys of the Yunling and Lancang rivers (IIAii-2a)
			Subdistrict of *Quercus glauca, Taiwania cryptomerioides*, and *Neyraudia reynaudiana* forests, tall grasses of the high and middle mountain valleys of the Gaoligong Mountain, Nujiang River, and Biluo Snow Mountain (IIAii-2b)
			Subdistrict of *Pinus yunnanensis* and *Tsuga dumosa* forests of the midmountain area of western Yunnan (IIAii-2c)
	Subregion of eastern (humid) evergreen broad-leaved forests	Zone of eastern (mid-sub-tropical zone) broad-leaved evergreen forests	District of *Castanopsis platyacantha* and *Lithocarpus cleistocarpus* forests along the midmountain valleys of northeastern Yunnan (IIBi-1)
			District of *Lithocarpus cleistocarpus, Castanopsis platyacantha,* and deciduous oak forests in the karst plateau of Zhenxiong (IIBi-2)
Region of Tibetan Plateau alpine vegetation	Subregion of Montane cold temperate coniferous forests in the southeast of the plateau	Zone of cold temperate coniferous forests and meadows at the south-eastern edge of the Qinghai–Tibet Plateau	District of *Picea asperata* and *Abies fabri* forests and *kobresia* sp., shrub meadows in Deqin and the off-mountain plateau of Zhongdian (IIIAi-1)

2.3. Forest Inventory Data Collection and Processing

Forest management inventory (FMI) data from 2016 were selected to obtain the oak forest AGBs. The distributions of the dominant species for the oak subcompartment patches were extracted, as shown in Figure 2. Then, the subcompartment data with storage volumes less than or equal to 0 m^3 were omitted. Moreover, abnormal subcompartments were also excluded using the triple standard deviation method. Finally, a total of 119,867 subcompartments were selected to estimate the oak forest AGBs using ArcGIS 10.8 software, and the statistical parameters of the subcompartment datasets for each vegetation district are shown in Figure 3.

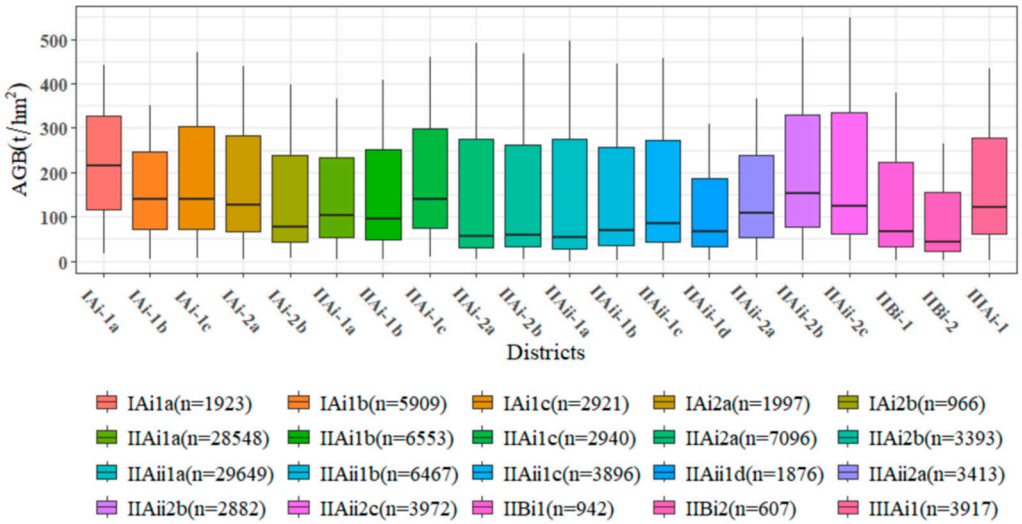

Figure 3. The basic parameters of the subcompartments in the 20 districts; n represents the number of subcompartments in the district.

Using the subcompartments of oak forests from 2016 FMI data, the AGB values per unit area were calculated using the biomass conversion variables method, as adopted by Xu et al. [43]. The parameters are listed in Table 2. The calculation formula was as follows:

$$B = V \times SVD \times BEF \quad (1)$$

where B is the AGB per unit area of the subcompartment (t/hm^2), V is the volume of storage per unit area in the subcompartment (m^3/hm^2), SVD is the basic wood density (t/m^3), and BEF is the biomass conversion factor (dimensionless).

Table 2. The parameters used with the biomass conversion factor method.

Forest	Age	*BEF*	*SVD* (t/m^3)
Oak	Young forest	1.3798	0.6760
	Half-mature forest	1.3947	
	Near-mature forest	1.2517	
	Mature forest	1.1087	
	Over-mature forest	1.1802	

2.4. Remote Sensing Data: Access and Processing

Landsat 8 Operational Land Imager (OLI) images from 2016 were downloaded from the website (http://www.gscloud.cn/ (accessed on 1 January 2022)), with a spatial resolution of 30 m (Table 3). Twenty-nine Landsat 8 OLI images, the majority with a cloud cover lower than 6%, were collected. Then, the remote sensing images were preprocessed by radiometric calibration, FLAASH atmospheric correction, topography correction, and geographic alignment in ENVI 5.3 software [29]. Radiometric calibration was carried out

to correct for sensor-specific variations in the raw data. Then, this study employed the FLAASH atmospheric correction module in the ENVI 5.3 software, which utilizes the MODTRAN5 radiative transfer model. This model effectively removes the impact of water vapor and aerosol scattering, providing high algorithmic accuracy. It also performs pixel-based corrections, addressing the "adjacent effect" between the target pixel and its neighbors [29]. In addition, topography correction was performed to address variations in the terrain height that could impact the reflectance values of the pixels. To enable accurate comparison and analysis, geographic alignment was also performed to align the images to a common coordinate system. Meanwhile, we utilized the Gram–Schmidt pan sharpening method within the ENVI 5.3 software suite for image enhancement, which helped us to maintain the spatial resolution in the overlapping regions. For the seamless integration of these images, we applied the seamless mosaic method, which is designed to mitigate issues of overlap by ensuring a smooth transition between tiles. Finally, we obtained the desired imagery of the study area (Figure 2).

Table 3. The parameters of 29 Landsat 8 OLI images.

No.	Image ID	Acquisition Date	Solar Elevation (°)	Solar Azimuth (°)	Mean Cloud Cover (%)
1	LC81330402016307LGN00	2 November 2016	42.8681	155.7033	1.56
2	LC81330412016323LGN00	18 November 2016	39.8182	156.6044	0.89
3	LC81320402016348LGN00	13 December 2016	34.2199	156.6774	0.73
4	LC81320412016348LGN00	13 December 2016	34.4429	156.0007	0.76
5	LC81320422016348LGN00	13 December 2016	36.6581	155.2988	0.32
6	LC81320432016012LGN02	12 January 2016	37.6659	150.1239	3.68
7	LC81300442016046LGN00	15 February 2016	45.3711	141.0448	0.01
8	LC81310412016325LGN01	20 November 2016	39.3429	156.6972	0.52
9	LC81310422016005LGN02	5 January 2016	36.0148	152.2167	0.05
10	LC81310432016325LGN01	20 November 2016	41.7926	155.1058	0.99
11	LC81310442016325LGN01	20 November 2016	42.9976	154.2569	4.57
12	LC81310452016069LGN00	9 March 2016	53.3872	132.1974	0.10
13	LC81300412016030LGN00	30 January 2016	38.2410	148.0217	1.28
14	LC81300422016030LGN01	30 January 2016	39.3315	147.1280	0.24
15	LC81300432016046LGN00	15 February 2016	44.3817	142.2120	2.22
16	LC81300442016046LGN00	15 February 2016	45.3711	141.0448	0.01
17	LC81300452016046LGN00	15 February 2016	46.3395	139.8293	0.01
18	LC81290402016151LGN00	30 May 2016	65.6228	119.6986	13.92
19	LC81290412016343LGN00	8 December 2016	36.0345	156.3999	2.22
20	LC81290422016327LGN00	22 November 2016	40.1300	155.9964	0.79
21	LC81290432016327LGN00	22 November 2016	41.3464	155.1964	0.15
22	LC81290442016039LGN00	8 February 2016	43.5143	142.9442	5.92
23	LC81290452016119LGN00	28 April 2016	66.7992	104.7207	1.22
24	LC81280412016208LGN00	26 July 2016	66.3707	104.7760	5.18
25	LC81280422016080LGN01	20 March 2016	54.6560	133.4815	4.31
26	LC81280432016128LGN00	7 May 2016	67.7248	105.7585	1.41
27	LC81280442016128LGN00	7 May 2016	67.8515	102.0989	13.36
28	LC81270432016041LGN00	10 February 2016	43.0065	143.5091	4.66
29	LC81270442016281LGN00	7 October 2016	55.0915	142.9570	4.64

2.5. Extracting Environment Factors

The climate data were downloaded from World-climate (http://www.worldclim.org/ (accessed on 1 January 2022)), and the spatial resolution was 1 km × 1 km. They were used to obtain 19 bio-climate variables. Soil data with 15 variables were obtained from the National Qinghai-Tibet Plateau Scientific Data Centre (https://www.tpdc.ac.cn (accessed on 1 January 2022)), and they were based on the soil data provided by the Nanjing Soil Institute of the Second National Land Survey, with a grid size of 1 km × 1 km. Digital Elevation Model (DEM) data were downloaded from the website (http://www.gscloud.cn/ (accessed on 1 January 2022)) with a spatial resolution of 30 m; then, 3 topography variables, including slope, aspect, and elevation, were generated and extracted from the DEM data. Finally, both the climate and soil data were resampled to 30 m to ensure a consistent image resolution among the datasets in ArcGIS 10.8.

Furthermore, according to the vegetation districts layer, we extracted 37 environmental variables, including 19 climate variables, 15 soil variables, and 3 topography variables, with the minimum, maximum, and mean, corresponding to the 20 vegetation districts (Table 4). Then, the values for the maximum variables, including the maximum temperature in the warmest month (MTW), precipitation in the wettest month (PWM), precipitation in the wettest quarter (PRW), and precipitation in the warmest quarter (PWQ), were extracted the maximum values from the climate data. The values for the minimum variables, including the minimum temperature in the coldest (MTC), precipitation in the driest month (PDM), precipitation in the driest quarter (PRD), and precipitation in the coldest quarter (PCQ), were extracted from the minimum values. The other 29 variables were extracted from the mean values.

Table 4. Overview of the 37 environmental variables.

Variables	Description	Variables	Description
AMTMean	The mean of annual mean temperature (°C)	BSTSMean	The mean of base saturation in the topsoil (%)
MDRMean	The mean of mean temperature diurnal range (°C)	CCFTMean	The mean of cation exchange capacity of the clay fraction in the topsoil (meq/100 g)
ISOMean	The mean of isothermality (%)	CECTMean	The mean of cation exchange capacity in the topsoil (meq/100 g)
TESMean	The mean of temperature seasonality (°C)	ESPTMean	The mean of exchangeable sodium percentage in the topsoil (%)
MTWMax	The max of maximum temperatures in the warmest month (°C)	PSATMean	The mean percentage of the sand in the topsoil (%)
MTCMin	The min of the minimum temperatures in the coldest month (°C)	PESTMean	The mean percentage of the silt in the topsoil (%)
TARMean	The mean of temperature annual range (°C)	TTVCMean	The mean of topsoil texture class Variables and code (-)
MTQMean	The mean of the mean temperatures in the wettest quarter (°C)	PECTMean	The mean of the percentage of clay in the topsoil (%)
MTDMean	The mean of the mean temperatures in the driest quarter (°C)	CCCTMean	The mean of calcium carbonate content in the topsoil (%)
MWQMean	The mean temperature in the warmest quarter (°C)	TRBDMean	The mean of topsoil reference bulk density (g/cm^3)
MCQMean	The mean of the mean temperatures in the coldest quarter (°C)	ELCTMean	The mean of electrical conductivity of the topsoil (S/m)
ANPMean	The mean of annual precipitation (mm)	VPGTMean	The mean volume percentage of the gravel in the topsoil (%)
PWMMax	The max of precipitation in the wettest month (mm)	POCTMean	The mean of the percentage of organic carbon in the topsoil (%)
PDMMin	The min of precipitation in the driest month (mm)	TOPHMean	The mean of topsoil pH (-)
PRSMean	The mean of precipitation seasonality (mm)	TEBTMean	The mean of total exchangeable bases in the topsoil (meq/100 g)
PRWMax	The max of precipitation in the wettest quarter (mm)	ELVMean	The mean elevation (m)
PRDMin	The min of precipitation in the driest quarter (mm)	SLOPEMean	The mean of the slope (-)
PWQMax	The max of precipitation in the warmest quarter (mm)	ASPECTMean	The mean of the aspect (°)
PCQMin	The min of precipitation in the coldest quarter (mm)		

2.6. Band Screening and Obtaining OSVs

The Green (Band2), Red (Band3), NIR (Band4), SWIR1 (Band5), and SWIR2 (Band7) bands of the Landsat Thematic Mapper (TM) had a stronger correlation with forest AGB, and the spherical model had better performance in remote sensing estimation for forest AGB [20]. Therefore, the 5 original bands, such as Blue (Band2), Green (Band3), Red (Band4), NIR (Band5), and SWIR2 (Band7), of Landsat 8 OLI were selected to analyze the Pearson correlation with the oak forest AGBs of 20 vegetation districts using the corrplot package in the R4.3.3 software. Then, the highest correlations of the bands were selected to obtain the OSVs of 20 vegetation districts using the spherical model in SPSS 23.0 software. The OSVs were calculated 20 times using 80% of the data in each vegetation district because of the uncertainty in calculating the OSVs; then, the average values of the OSVs in each vegetation district were used to analyze the variation. The formula for the spherical model is as follows:

$$y(AGB) = \begin{cases} c_0 + c\left(\frac{3AGB}{2OSV} - \frac{AGB^3}{2OSV^3}\right) & 0 \le \text{AGB} \le \text{OSV} \\ c_0 + \text{c} & \text{AGB} > \text{OSV} \end{cases} \quad (2)$$

where Y(AGB) is the spectral reflectance value; c_0 is the value of the spectral reflectance when the biomass value is 0; c is the spectral rate of change; $c_0 + c$ is the maximum or minimum value of the spectral reflectance when the biomass is saturated; and OSV is the optical saturation value of the spectral bands in forest AGB estimation. If $b_0 = c_0$, $b_1 = \frac{3c}{2OSV}$, $b_2 = -\frac{c}{2OSV^3}$, and x = AGB, it could be solved using least squares regression, as follows:

$$y = b_0 + b_1 x + b_2 x^3 \quad (3)$$

By applying least squares fitting to Equation (3) to solve for the parameters in Equations (4) and (5), the OSVs are finally calculated using the combination of parameters b_1 and b_2 in Equation (6), as follows:

$$b_1 + b_2 = \frac{3c}{2\text{OSV}} - \frac{C}{2\text{OSV}^3} \quad (4)$$

$$\text{c} = \frac{2}{3}\text{OSV} \times b_1 \quad (5)$$

$$\text{OSV} = \sqrt{-\frac{b_1}{3b_2}} \quad (6)$$

2.7. OSV Variation Analysis and Environmental Interpretation

2.7.1. Environmental Variables Screening

Numerous studies have demonstrated the critical role of selecting appropriate variables in enhancing model estimation accuracy [2]. Random forests (RFs) have been widely employed for variable screening based on the comprehensive ranking of %IncMSE and IncNodePurity after determining the optimal combination of ntree and mtry [44]. In this study, we used a stable RF model in which the ntree was 300, the mtry was 2, the maximum number of iterations was 200, the max-depth was 10, the min-samples-leaf was 1, and the min-samples-split was 2. Then, the RF model was used for the variables screening to select the superior variables with OSVs from 37 environmental variables. Ultimately, the relationships between the selected environmental variables and OSVs were analyzed using Pearson correlation analysis in the corrplot package of R software.

2.7.2. Analysis of the Environment Effect on OSV Variation

The partial least squares structural equation model (PLS-SEM) is considered a powerful tool for analyzing causal relationships and testing theoretical models [45]. The PLS-SEM was used to clarify the relationship between the environmental variables and the OSV variation for the oak forests in Yunnan with the plspm package in the R software. First, the selected environmental variables were standardized to eliminate the influences of

differences in units and variances, which can enhance the reliability and accuracy of the results and achieve equal weights and comparability among variables. Then, the standardized data were used to construct the PLS-SEM to evaluate causal pathways and the model accuracy [46]. The relationships among OSVs, soil, topography, and climate variables, as well as the interactive and comprehensive effect of three environmental factors, were quantified. The individual effects and interactive effects among the three environmental factors on the OSV variation were analyzed using the path coefficient of causal pathways. Meanwhile, when calculating the comprehensive effects, all of the selected higher correlation variables were used to construct the SEM model to clarify the comprehensive effect coefficient with the OSVs.

The coefficient of determination (R^2), average variance extracted (AVE), comparative fit index (CFI), and root mean square error of approximation (RMSEA) were used for model validation in this study. The equations are all listed below, as follows:

$$R^2 = 1 - \frac{\sum_{i=1}^{n} (y_i - \hat{y}_i)^2}{\sum_{i=1}^{n} (y_i - \overline{y}_i)^2} \quad (7)$$

$$AVE = 1 + \frac{\sum \lambda^2}{\sum \sigma} \quad (8)$$

$$GFI = 1 - \frac{tr\left[\left(E^{-1}S - I\right)^2\right]}{tr\left[\left(E^{-1}S\right)^2\right]} \quad (9)$$

$$RMSEA = \sqrt{\frac{\chi^2 - df}{df(n-1)}} \quad (10)$$

where y_i is the measured value, $\hat{y}_i$ is the inversion value, $\overline{y}_i$ is the mean of the measured value, n is the number of samples, λ^2 is the square of the standardized factor loadings, σ is the standard deviation of the observed variables, S is the sample covariance matrix, E is the regenerated covariance matrix, χ^2 is the test statistic of the model, and df is the degrees of freedom in the models.

3. Results

3.1. Correlation between the Bands and Oak Forest AGB

The correlation analysis results are shown in Figure 4. They indicate that all bands were negatively correlated with the oak forest AGBs, and the majority of the correlation coefficients were significant correlations with the oak forest AGBs. Moreover, the red and SWIR2 bands had significantly higher correlations with the oak forest AGBs in the 20 vegetation districts, and the red band was better correlated in the whole study area. Then, we conducted a significant difference test on the correlations between the oak forest AGBs and the bands. As shown in Figure 5, the significances of the differences varied among the single bands. For example, for the red band, there were significant differences compared with the green and SWIR1 bands, while the differences for the SWIR2 and red bands were not significant. Therefore, using the spherical model, we chose the red band to estimate the OSVs of the 20 vegetation districts.

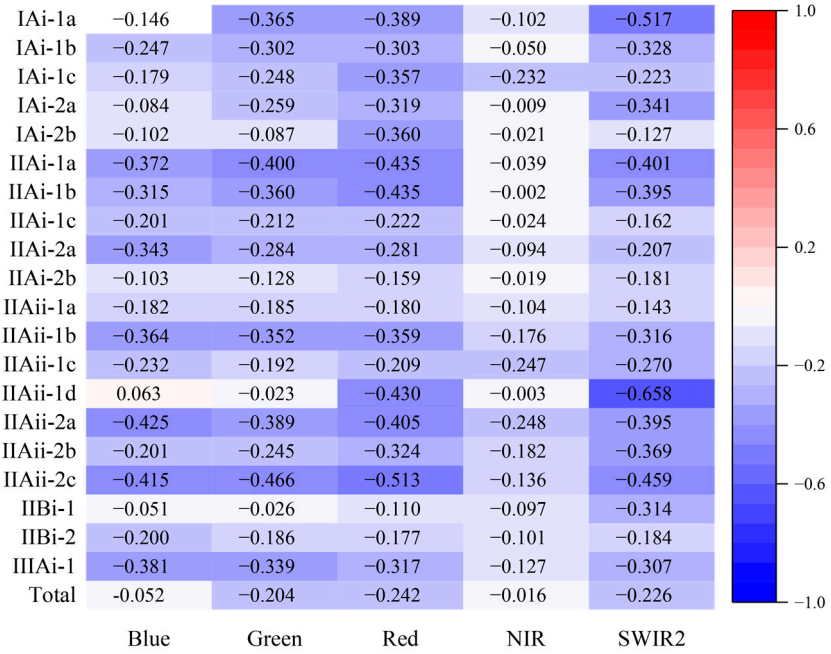

Figure 4. Correlation between oak forest AGBs and the original bands.

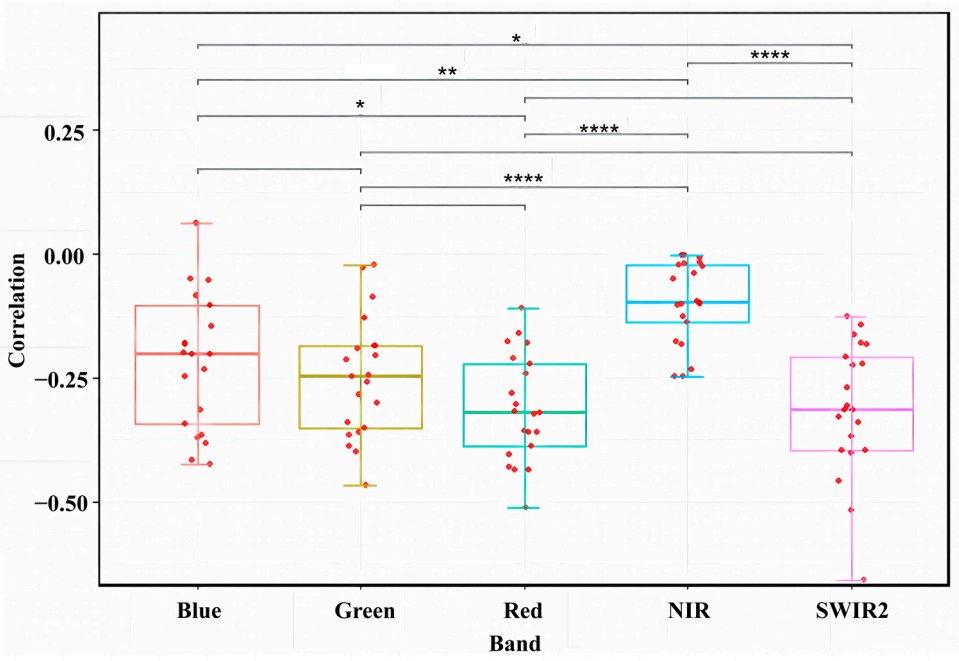

Figure 5. Correlation between various bands and oak forests AGBs, as well as the significance test results for the correlations of the various bands. COR is the correlation between bands and oak forest AGBs; B is the image bands. **** Represents significance (i.e., $p < 0.0001$), ** represents significance (i.e., $p < 0.01$), and * represents significance (i.e., $p < 0.05$).

3.2. Variation Analysis of the OSVs

As shown in Figure 6, the variation in each OSV in each district was relatively uniform, and the average OSV was close to the median, suggesting that there were minimal differences in OSVs across these areas. Moreover, as shown in Figure 7, it can be found that the range of OSVs was 104 t/hm^2 to 182 t/hm^2 for the oak forests in Yunnan province, and the largest value was 181.5 t/hm^2 in the subdistrict of *Antiaris toxicaria*, *Pouteria grandifolia*, *Canarium subulatum*, *Ficus altissima*, and *Chukrasia tabularis* forests in the southern midmoun-

tain basin of Xishuangbanna (IAi-1a). On the contrary, the smallest value was 104.33 t/hm^2 in the subdistrict of *Pinus yunnanensis*, *Castanopsis orthacantha*, and *Abies fabri* forests in the high and middle mountain valleys of the Yunling and Lancang rivers (IIAii-2a). The OSVs of most districts were from 130 t/hm^2 to 160 t/hm^2, and small parts of the districts had OSVs from 104 t/hm^2 to 130 t/hm^2 or 160 t/hm^2 to 182 t/hm^2 in general. Overall, the OSVs were various, with trends of being lower in northeastern and western Yunnan, higher in northwestern, southeastern, and central Yunnan, and the highest in southern Yunnan.

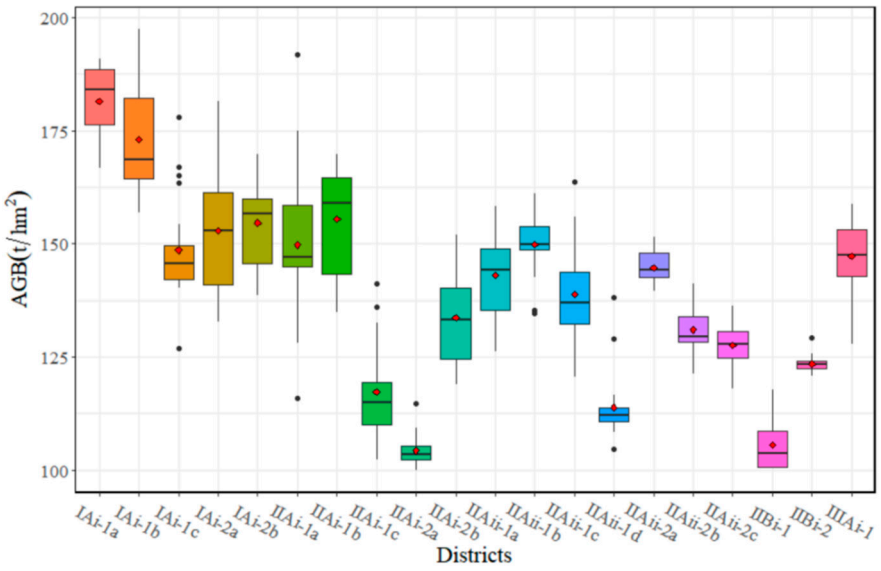

Figure 6. The mean OSVs calculated by the red band in the 20 vegetation districts. The black points represent the outlier data, and the red points represent the average values.

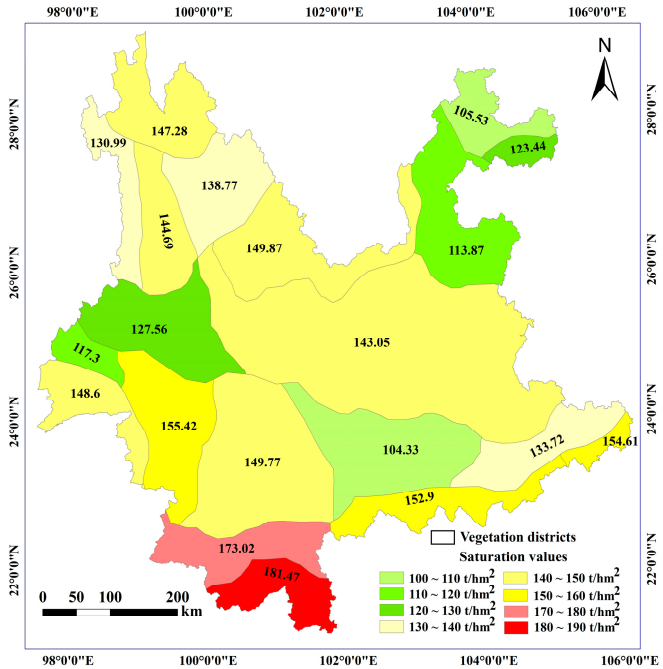

Figure 7. The OSVs obtained by the red band in the 20 vegetation districts.

3.3. Relationships between the Environmental Factors and OSV Variation

As shown in Figure 8, the largest %INCMSE in the mean cation exchange capacity of the clay fraction in the topsoil (CCFTMean) was 15.98%, the mean of the mean temperature

diurnal range (MDRMean) was 8.84%, and the mean elevation of the Digital Elevation Model (ELVMean) was 8.86%. The maximum IncNodePurity of the mean percentage of the clay in the topsoil (PESTMean) was 415.87, the max of the maximum temperatures of the warmest month (MTWMax) was 410.63, and the ELVMean was 285.52. Finally, 15 variables were selected by composing the IncNodePurity and %INCMSE, such as MDRMean, the mean of the temperature seasonality (TESMean), MTWMax, the mean of the mean temperature in the coldest quarter (MCQMean), the mean of the annual precipitation (ANPMean), the min of the precipitation in the coldest quarter (PCQMin), the mean annual mean temperature (AMTMean), the mean of isothermality (ISOMean), the max of the precipitation in the wettest month (PWMMax), CCFTMean, PESTMean, the mean of the topsoil pH (TOPHMean), the mean of the topsoil texture class variables and code (TTVCMean), ELVMean, and the mean of the slope (SLOPEMean) variables.

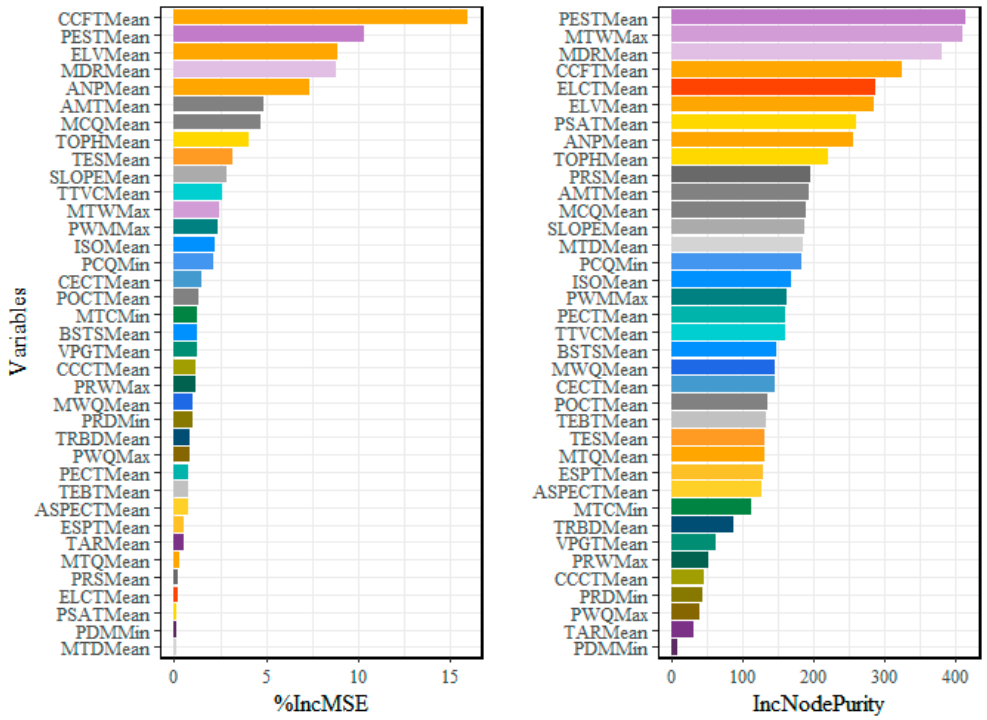

Figure 8. The variables were screened using the mean square error (%IncMSE) and the total reduction in node impurity (IncNodePurity) of the RF model.

Afterward, the relationships between the OSVs and the 15 selected environment variables in the 20 vegetation districts were quantified by Pearson correlation analysis. As shown in Figure 9, it was evident that seven variables, namely, TESMean, CCFTMean, PESTMean, TOPHMean, TTVCMean, ELVMean, and SLOPEMean, displayed a negative correlation with the OSVs. In contrast, eight variables, including MDRMean, MTWMax, MCQMean, ANPMean, PCQMin, AMTMean, ISOMean, and PWMMax, exhibited a positive correlation. The correlations indicate that the effect of each environmental variable on the OSVs was different, which is meaningful for the analysis of OSV variation concerning the topography, climate, and soil individually.

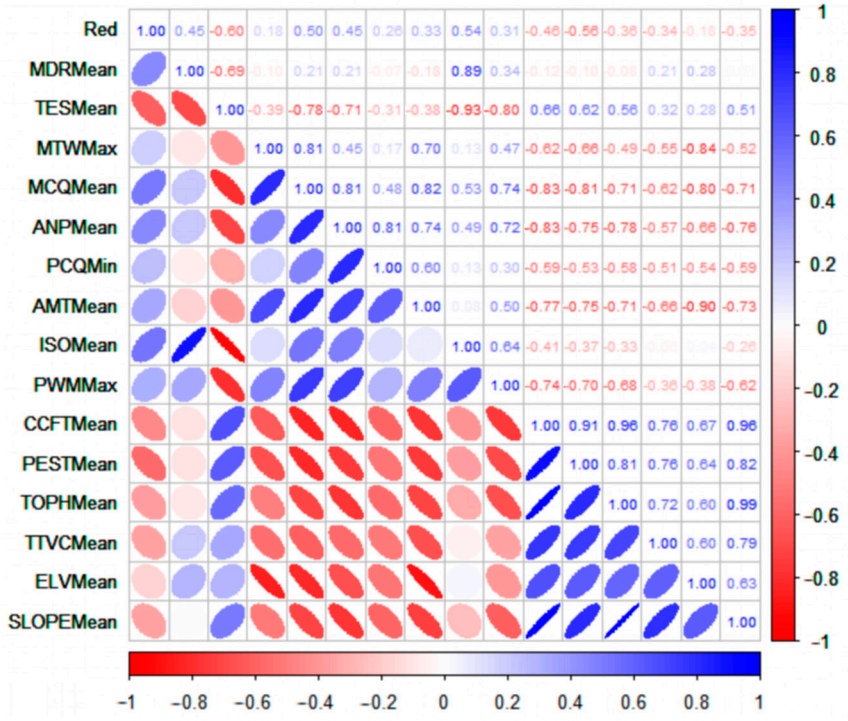

Figure 9. The correlations between the OSVs and environmental variables.

As Table 5 shows, the model's performance exhibited a high GFI of 0.909 and a low RMSEA of 0.045. The climate factor was the only exogenous variable in the model, and the R^2 value was 0, which indicate that climate affected the endogenous variables in the model. Alternatively, the R^2 of the environment variable was 1, indicating that it was a composite variable of other endogenous variables, and its variance can be entirely accounted for by other latent variables. The OSVs showed the highest consistency with an AVE of 1 due to a very high proportion of shared variance between the latent variable and its corresponding observed indicators, indicating that the latent variable was very reliable and effective in the model.

Table 5. Reliability and validity assessment of the PLS-SEM model. Average variance extracted (AVE), goodness of fit index (GFI), and root mean square error of approximation (RMSEA). R^2 is the proportion of the explained variance of each endogenous variable in the model.

Variables	Types	Size	R^2	AVE	GFI	RMSEA
Climate	Exogenous	9	0.000	0.565		
Topography	Endogenous	2	0.560	0.985		
Soil	Endogenous	4	0.940	0.866	0.909	0.045
OSVs	Endogenous	1	0.367	1.000		
Environment	Endogenous	15	1.000	0.625		

As illustrated in Figure 10, the topography and climate factors showed positive correlations with the OSVs, while the soil factor exhibited a negative correlation. The results show that the soil factor had the greatest direct and total impact on the OSVs, with a coefficient of −0.635, which had no indirect effect on the OSVs. The direct effect of the climate factor was 0.346, the total effect was 0.517, and the indirect effect could be calculated as 0.171. The topography had the highest indirect effect, with a value of −0.475, and the direct and total effects of the topography factor were 0.879 and 0.404, respectively. Furthermore, 15 variables, except TESMean, showed positive correlations with the OSVs. MCQMin demonstrated the strongest positive correlation at 0.958 among the climate variables, CCFTMean exhibited the highest coefficient value at 0.983 for the soil variables, and ELVMean

was 0.983 among the topography variables. Therefore, the highest total correlation coefficient for CCFTMean with the OSVs was observed for the soil factor at −0.624. The highest total correlation coefficient of MCQMean was found to be 0.495 for the climate factor, while the highest total correlation coefficient of ELVMean was observed to be 0.401 for the topography factor.

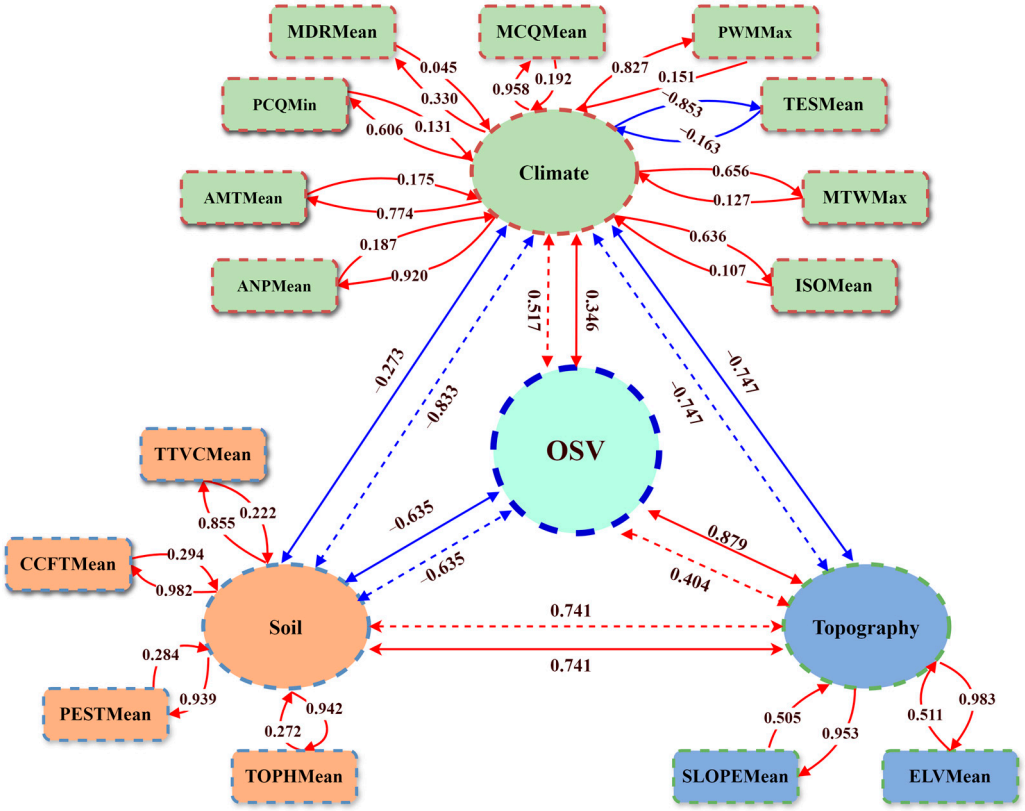

Figure 10. The individual effects of climate, soil, and topography factors on the OSV variation. The red solid line represents a direct positive effect among variables, while the red dashed line represents the total positive effect of variables that are positively correlated. The blue solid line represents a direct negative effect among variables, while the blue dashed line represents the total negative effect of variables that are negatively correlated. The indirect effect is equal to the overall effect minus the direct effect. The red curve represents a positive correlation among variables, while the blue curve represents a negative correlation among variables.

In addition, the environmental factors always interacted and affected each other. The direct correlation coefficient between the climate and soil factors was −0.273, the total effect was −0.833, and the indirect effect was −0.560. The direct and total effects between the climate and topography factors were both −0.747. The direct and total effects between the soil and topography factors were the same at 0.741. The total correlation coefficients among the environmental factors were all greater than 0.7, indicating a strong level of interaction among the environmental factors. As shown in Figure 11, the comprehensive effect of the three environmental factors had both direct and total effects on the OSVs, and the correlation coefficient was 0.436. In the comprehensive effect analysis, it was found that the climate factor had the highest total effect (0.949) among the three factors, followed by the soil factor at −0.456 and the topography factor at −0.352. These results indicate that the climate factor (0.414) had the most significant contribution to the comprehensive effect on the OSV variation, followed by the soil factor (−0.199) and the topography factor (−0.153). Therefore, the MCQMean, ANPMean, and CCFTMean variables were identified as the top three variables with the highest comprehensive effect on the OSVs, and the values were

0.416, 0.409, and −0.404. The ELVMean variable had a correlation coefficient of −0.399 in the topography factor, ranking it fifth out of the 15 selected variables.

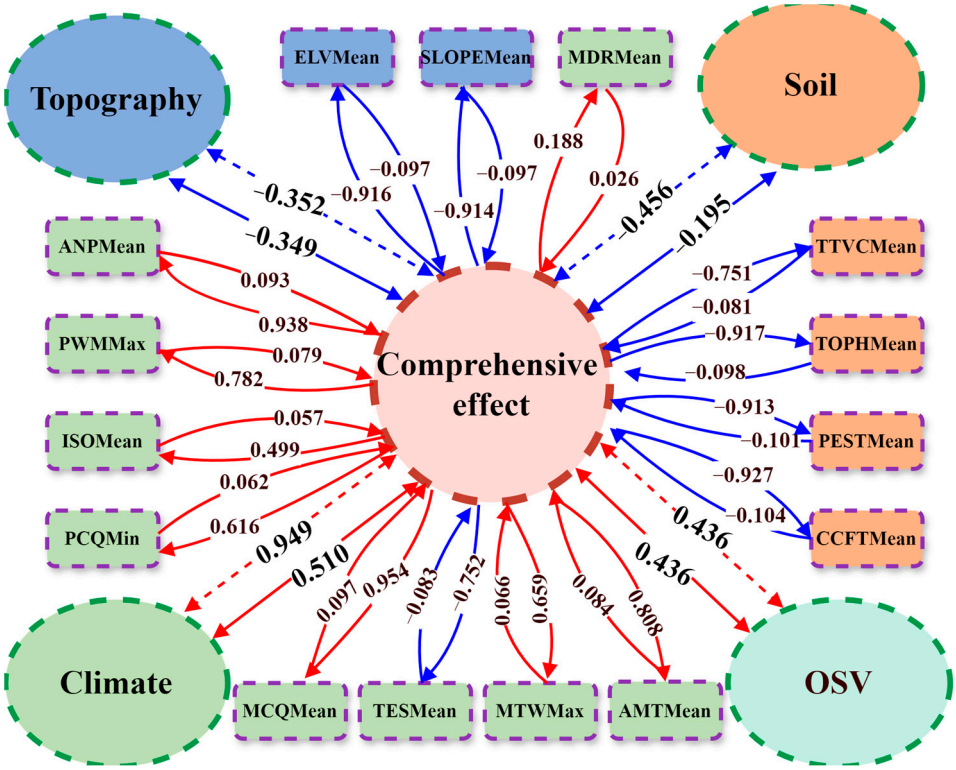

Figure 11. The comprehensive effects of the three environmental factors on the OSVs. The meanings of the graphic elements are explained in Figure 10.

4. Discussion

4.1. OSV Variation

There was a negative correlation between the original bands and oak forest AGBs according to the Pearson correlation analysis in this study. A higher vegetation coverage leads to lower electromagnetic radiation signals in the original bands of the Landsat 8 OLI [2,47]. This indicates that the bands of the Landsat 8 OLI measure electromagnetic radiation signals, which show an inverse correlation between vegetation leaf coverage and AGB [48].

Moreover, the red and SWIR2 bands of the Landsat 8 OLI exhibited stronger correlations with AGB in estimating the OSVs. Their sensitivity to land cover type and vegetation growth status, coupled with their relatively low susceptibility to atmospheric interference, can be clarified [49]. Green vegetation absorbs and reflects less red light, and the reflectance in the red band can provide valuable information about the density and productivity of vegetation [14]. It reflects light from the surface, which can be used to determine the type and density of the vegetation coverage, attributed to the chlorophyll-absorbing red band which becomes insensitive to light with increasing vegetation canopy closure [19]. Thus, the SWIR2 band had higher correlations with the vegetation structure and water content, and it was less affected by atmospheric interference [50]. This is similar to the results of Zhao et al. [20], who found that the SWIR2 band had a stronger correlation with AGB.

We used the red band and obtained the OSVs at a range of 104 t/hm^2 to 182 t/hm^2 for the oak forests of 20 districts in Yunnan province. Similarly, the OSVs of different vegetation types in Zhejiang province were in the range of 100 t/hm^2 to 159 t/hm^2 using the SWIR2 band of the Landsat TM [20]. There were higher OSVs for oak forests in Yunnan compared to the broadleaf forests in Zhejiang province. The difference can be attributed to the fact that Yunnan province is characterized by complex mountain and highland topography and high

forest heterogeneity [39]. Previous studies have demonstrated that complex forest stand structures, various vegetation types, and diverse biophysical environments, particularly in regions with high forest heterogeneity, exhibit a more pronounced saturation problem and larger OSVs [2,22].

Simultaneously, we also used the SWIR2 band to obtain the oak forest OSVs in Yunnan province. As shown in Figure 12, the OSV was the largest in the subdistrict of *Terminalia myriocarpa*, *Pometia pinnata*, *Semecarpus albescens*, and *Machilus nanmu* forests in the northern midmountain basin of Xishuangbanna (IAi-1b) at 175.39 t/hm^2, and it was the smallest in the subdistrict of *Pinus yunnanensis* and *Schima wallichii* forests and *Bombax ceiba* and *Woodfordia fruticosa* bushes in the karst plateau valley of Mengzi and Yuanjiang (IIAi-2a) at 104.99 t/hm^2. Therefore, the variation in the different districts was approximately the same when comparing the OSVs obtained by the red and SWIR2 bands in this study, and this indicates that OSV variation exists objectively, to some extent.

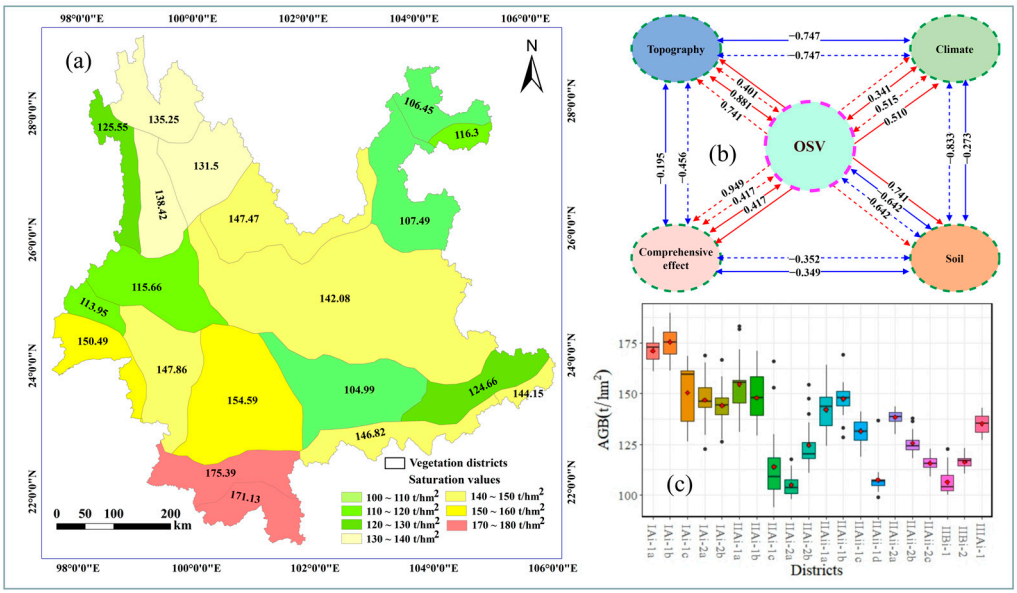

Figure 12. The OSV variation and environmental interpretation by the SWIR2 band for the oak forests in Yunnan province: (**a**) OSVs of the oak forests in the 20 vegetation districts; (**b**) relationships among the comprehensive effects of the three environmental factors on the OSV variation from the PLS-SEM model; (**c**) OSVs calculated by the SWIR2 band in the 20 vegetation districts.

4.2. Individual Environment Effect on OSV Variation

It was shown that the three environmental factors had a significant individual effect on the OSVs in the PLS-SEM model. The ranking of the total effects on the OSV variation for the three environmental factors is soil > climate > topography, which indicates that the soil factor had the highest effect on the OSVs. As shown in Figure 12, we also obtained similar results for the OSVs calculated by the SWIR2 band. Furthermore, there was only a direct effect between soil and OSVs. The soil factors were the critical ones affecting the distribution of tree species [51]. The absence of an indirect effect between the soil factor and OSVs could be attributed to the fact that soil primarily affects physical and chemical properties, as well as the structure, of the soil itself [52]. The climate and topography factors also had a direct effect on the OSV variation. Climate can directly affect the vegetation types, distribution of trees, and photosynthesis of plants. Meanwhile, climate change can affect forests by altering the frequency, intensity, duration, etc. [53]. The topography, such as elevation, slope, and aspect, can directly affect species composition and tree growth [54]. Therefore, the three environmental factors directly impact the forest types, stand structures, and biomass allocation [55], which then leads to OSV variation.

Except for direct effects, both the topography and climate factors had indirect effects on the OSV variation in this study by affecting soil formation, soil properties, and soil quality [56]. Moreover, the key environmental factors with higher correlation coefficients with the OSVs can be found in this study. The CCFTMean had the strongest correlation impact on the OSVs, and the reason might be that the soil fertility and nutrient supply capacity were measured by the average cation exchange capacity [57]. This relationship may be explained by the fact that as the mean cation exchange capacity of the clay fraction in the topsoil increases, more cations in the soil are likely to be bound to clay minerals and organic matter, making it more challenging for plants to access nutrients [58]. Oak forests thrive in soils that are neutral to slightly acidic [59]. An excessively high cation exchange capacity may lead to the soil becoming too alkaline, which is not suitable for the growth and development of oak forests, ultimately, resulting in a decrease in OSVs [60].

4.3. Interactive Effect of Environmental Factors on the OSV Variation

Soil, climate, and topography engage in intricate relationships, with each correlation coefficient surpassing 0.7. Notably, the most prominent interaction occurs between soil and climate, boasting a correlation coefficient of −0.833. A parallel zonal distribution emerges for both the soil and climate factors [61], and the interactive effect between both of these environmental factors can affect tree composition and plant growth and, thus, community structure and biomass allocation, and, ultimately, even the health and stability of the entire ecosystem [62]. Especially with the strongest negative correlation between soil and climate, the distribution of tree species and forest structures exhibited a complex yet ordered pattern in the environment. A deeper comprehension of the dynamic changes in tree species distribution and forest structure will offer crucial insights into understanding the variability of optical saturation values.

Furthermore, delving into a more profound understanding, we uncovered an additional layer of interaction between topography and soil. Topography exerts a substantial influence on the formation and distribution of soil, forming a dynamic interplay whereby the quality and characteristics of the soil reciprocally affect the topography [63]. Specifically, various topographical features, such as elevation, slope, and aspect, play a pivotal role in shaping the physical, chemical, and biological attributes of the soil, encompassing factors like texture, moisture, and nutrient content [64]. These alterations in soil characteristics, in turn, have far-reaching consequences, impacting the distribution of forest types and stand structures. This intricate interplay cascades through the ecosystem, leading to consequential variations in optical saturation values (OSVs). As a result, the interwoven relationships between topography and soil dynamics contribute significantly to a comprehensive understanding of environmental influences on OSV variability.

In addition, the interactive effects between climate and topography factors are complex and multidimensional processes. Climate factors play a pivotal role in shaping diverse topographies and geographical features, while topography, in return, exerts an influence on the distribution and characteristics of the climate [65]. Specifically, this indicates increases in erosional efficiency in wetter, more humid climates, lowering the relief rate, resulting in the topography [31]. Therefore, the mutual interaction and regulation between climate and topography factors collectively mold a wide range of topography features, climate distribution patterns, and types of forests [66], which are then responsible for the variations in OSV.

4.4. Comprehensive Effect of Environmental Factors on the OSV Variation

In this study, the OSVs were <130 t/hm^2 in the IIAii-2a; the district of *Castanopsis platyacantha* and *Lithocarpus cleistocarpus* forests along the midmountain valleys of northeastern Yunnan (IIBi-1); the district of *Lithocarpus cleistocarpus*, *Castanopsis platyacantha*, and deciduous oak forests in the karst plateau of Zhenxiong (IIBi-2); the subdistrict of *Leymus chinensis* meadow and *Pinus yunnanensis* forest in the high and middle areas of the northeastern Yunnan plateau (IIAii-1d); the subdistrict of *Pinus yunnanensis* and *Tsuga*

dumosa forests in the midmountains of western Yunnan (IIAii-2c); and the subdistrict of *Castanopsis ferox*, *Castanopsis hystrix*, and *Lithocarpus truncatus* forests in the midmountainous plateaus of Longling and Lianghe (IIAi-1c), which are located in typical arid valleys and regions in Yunnan. Arid valleys and regions have greater evaporation, which results in variations in tree species composition and stand structures, causing variation in the biomass allocation of the oak forests [67] and, thus, to variations in OSVs. The OSVs were > 160 t/hm^2 in IAi-1a and the subdistrict of *Terminalia myriocarpa*, *Pometia pinnata* forests, *Semecarpus albescens*, and *Machilus nanmu* forests of the northern midmountain basin of Xishuangbanna (IAi-1b), which are located in tropical regions with higher levels of humidity and temperatures, and this can result in higher forest heterogeneity, affecting the variation in the OSV [68]. Thus, we found that the comprehensive effect among the three environmental factors had a common impact on the OSVs by affecting the humidity levels and temperatures of the districts [69]. Furthermore, climate factors, for instance, affected temperature, precipitation, and evapotranspiration, which in turn affected soil moisture and water cycling [70]. Topography features affected the soil moisture by influencing the water flow and accumulation [71], and the temperature decreased with the increase in altitude [72]. Meanwhile, humidity and temperature can affect the chlorophyll content, structure, and water in leaves, resulting in the various reflectance values of the red and SWIR2 bands [73]. As shown in Figure 13, the reflectance values of the original bands varied in each district, although with the same OSV.

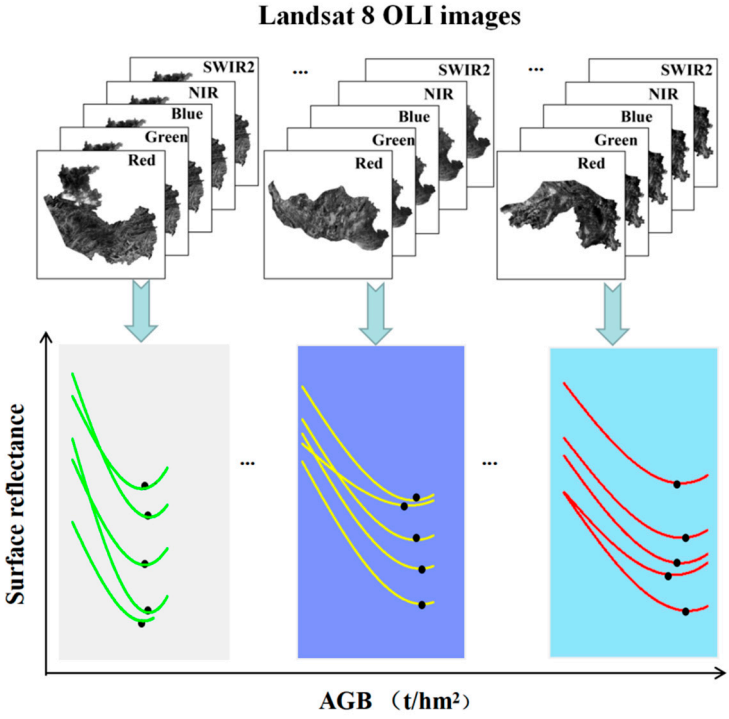

Figure 13. The relationship between the OSVs and the reflectances of the original bands.

Therefore, the three factors affected the variation in the forest types and AGB distributions comprehensively, which resulted in the variation in the OSV distributions [74]. The climate factor had the highest comprehensive effect on the OSV variation, with a correlation coefficient of 0.414, followed by the soil factor at −0.199 and the topography factor at −0.153. This can be attributed to the fact that climate factors have the most substantial and direct effects on temperature and humidity, whereas the roles of topography and soil were relatively insignificant [75]. The comprehensive effect of the climate factors directly affected the plant physiological processes, growth rates, and biomass accumulation, as well as indirectly influenced vegetation type distribution and long-term climate trends, thereby exerting a significant impact on OSV variation [53]. The soil and topography

factors showed a negative correlation with the OSVs, which may be due to the combined effects of the water drainage and water-holding capacity, nutrient supply and soil quality, soil permeability, and root development, as well as elevation and topographical humidity. Different soil types and topography features can restrict water availability, nutrient uptake, and plant growth, thereby influencing the estimation of OSVs [76]. Furthermore, the MCQMean had the highest comprehensive effect (0.416) on the OSV variation, and there was a higher proportion of cold-adapted species in the areas with lower MCQ values [32]. The plant species may have different biomass accumulation patterns or growth rates compared to species found in areas with higher MCQ values [77]. Nevertheless, oak forests are a positive tree group, which prefers a mild environment. Therefore, a higher MCQMean may result in a higher OSV. Meanwhile, the average annual precipitation (ANPMean) also had a significant effect on the OSVs, reflecting the variations in precipitation that had a profound influence on the growth and development of vegetation types. Adequate precipitation is generally favorable for plant growth, leading to biomass production increases, as well as affecting variations in OSVs [78].

Moreover, the ELVMean variable positively affected the OSV variation in the individual effect analysis but negatively in the comprehensive effect analysis. As shown in Figure 14, a linear negative correlation was found between ELVMean and the OSVs from an overall perspective. But we can also see that the relationship between ELVMean and the OSVs was nonlinear, exhibiting a repetitive pattern of initially increasing and then decreasing, which may be attributed to environmental heterogeneity [41,79].

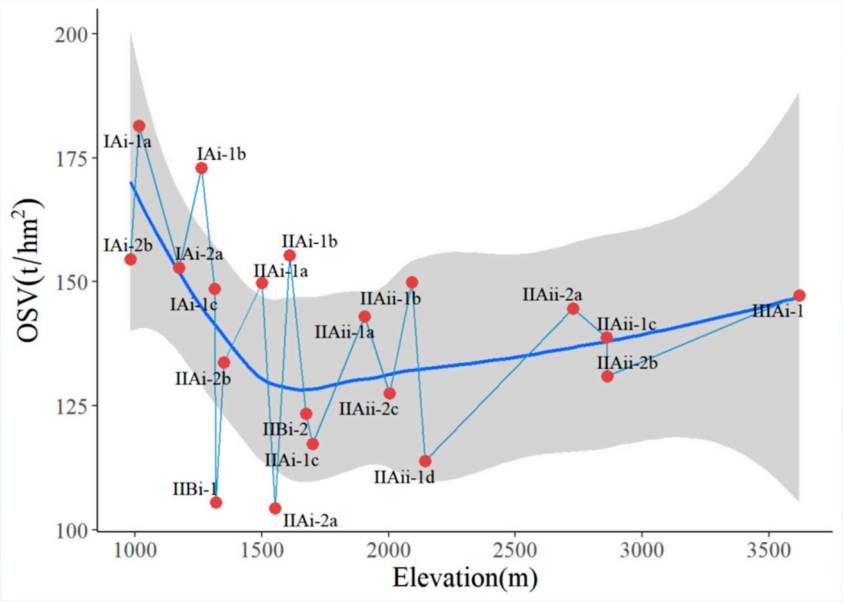

Figure 14. The OSVs and mean elevation of each vegetation district, the blue curve line represents the fitting trend and the grey area denotes the 95% confidence interval.

Overall, it was concluded that the OSV variations for oak forests in Yunnan are caused by the comprehensive effects of three environmental factors, and those effects can affect the species composition, stand structure, forest heterogeneity, and biomass allocation, ultimately, leading to variations in the OSVs.

4.5. Application and Future Research

The individual, interactive, and comprehensive effects of three environmental factors significantly affected the OSV variations, and the primary environment variables influencing the OSVs were identified in this study. There is some research that has identified environment variables that could reduce the uncertainty of the saturation problem and improve the accuracy of forest AGB estimation [15]. For instance, Hernández et al. [80] and

Fu et al. [81] incorporated climate variables to reduce the uncertainty caused by saturation and improve the accuracy of tree AGB estimations. Shao et al. [82] found that soil variables significantly enhance the accuracy of estimating forest AGBs by incorporating site productivity measures into lidar-based models, particularly for temperate hardwood forests. Meanwhile, Zhou et al. [83] clarified that topographical variables, when combined with high-resolution optical data and texture information, significantly improve the accuracy of estimating forest AGBs, showcasing the benefit of integrating diverse data types. Therefore, incorporating environmental factors may reduce the uncertainty caused by optical saturation in forest AGB estimations, especially the key variables. However, how well the inclusion of environmental variables reduces the effect of optical saturation and, thus, improves forest AGB estimation accuracy, especially on the provincial scale, for which the terrain is complex, needs to be further investigated.

Moreover, we estimated the OSVs of the oak forests using Landsat 8 OLI images and explored the environmental effects. Other optical images, such as from Sentinel-2, SPOT, MODIS, QuickBird, ASTER, and AVHRR, were used to estimate forest AGBs on a large scale [84]. Coniferous forests and the other broad-leaved forests are distributed widely. Thus, it is necessary to explore OSV variations and environmental effects for other forest types using more optical remote sensing imagery in further research.

5. Conclusions

To clarify the variations in OSVs of forest AGB estimations using optical remote sensing data and explore the environmental effects on the OSV variations, in this study, the OSVs of oak forest AGB estimations using Landsat 8 OLI imagery were obtained by the spherical model, and the OSV variation was analyzed for 20 vegetation districts of Yunnan province, China. Then, using the random forests models, the main environmental variables affecting the OSV variations in different vegetation districts were obtained from the three environmental factors of climate, soil, and topography. Finally, the individual, interactive, and comprehensive effects of the three environmental factors on the OSV variations were clarified by the PLS-SEM model. The conclusions of this study are as follows:

(1) The red band was used to calculate the OSVs because it had a stronger correlation with oak forest AGBs. The range of OSVs was from 104 t/hm^2 to 182 t/hm^2. The OSVs were lower in northeastern and western Yunnan, and the highest OSVs were in southern Yunnan.
(2) In the individual effect analysis, the soil factor had the greatest individual effect on the OSV variation, with a correlation coefficient of −0.635, followed by the climate factor at 0.517 and the topography factor at 0.404.
(3) There was a strong interaction effect among the three environmental factors, and the absolute value of the correlation coefficients exceeded 0.7. The interactive effects can affect forest stand structures, leading to variations in the OSVs.
(4) It was evident that the three environmental factors had a strong comprehensive effect (0.436) on the OSVs. The climate factor had the highest effect (0.414) on the OSVs, followed by the soil factor (−0.199) and the topography factor (−0.153). The MCQMean variable showed the highest comprehensive correlation (0.416) with the OSVs.

In summary, the individual, interactive, and comprehensive effect of the three environmental factors on the OSV variation was significant in the AGB estimations of oak forests using Landsat 8 OLI images by the PLS-SEM model. Quantified environmental effects can help to understand the variations in OSVs, providing a good reference to improve the accuracy of forest AGB estimations using optical remote sensing on a large scale.

Author Contributions: Y.W., participated in the collection of the data, conducted the data analysis, and wrote the draft of the paper; T.H., X.Z., C.L. (Chunxiao Liu), Z.L., Z.Y., H.L., C.L. (Chi Lu) and K.S., helped with the data analysis and part of the graphs; L.W. and W.X., provided suggestions and guidance; G.O., supervised and coordinated the research project, designed the experiment, and revised the paper. All authors have read and agreed to the published version of the manuscript.

Funding: This research was jointly supported by the Key Research and Development Program of Yunnan Province, China (202303AC100009), the Scientific Research Fund Project of Yunnan Provincial Education Department (2023Y0732), the Ten Thousand Talent Plans for Young Top-Notch Talent of Yunnan Province (YNWR-QNBJ-2018-184), and the Education Talent of Xingdian Talent Support Program of Yunnan Province, China.

Data Availability Statement: The original contributions presented in this study are included in the article, further inquiries can be directed to the corresponding author.

Acknowledgments: We would like to acknowledge all of the people who scontributed to this paper.

Conflicts of Interest: The authors declare no conflict of interest.

References

1. Chen, G.; Zhang, X.; Liu, C.; Liu, C.; Xu, H.; Ou, G. Error Analysis on the Five Stand Biomass Growth Estimation Methods for a Sub-Alpine Natural Pine Forest in Yunnan, Southwestern China. *Forests* **2022**, *13*, 1637. [CrossRef]
2. Lu, D.; Chen, Q.; Wang, G.; Liu, L.; Li, G.; Moran, E. A survey of remote sensing-based aboveground biomass estimation methods in forest ecosystems. *Int. J. Digit. Earth* **2016**, *9*, 63–105. [CrossRef]
3. Hu, T.; Zhang, Y.; Su, Y.; Zheng, Y.; Lin, G.; Guo, Q. Mapping the global mangrove forest aboveground biomass using multisource remote sensing data. *Remote Sens.* **2020**, *12*, 1690. [CrossRef]
4. Zhou, F.; Zhong, D. Kalman filter method for generating time-series synthetic Landsat images and their uncertainty from Landsat and MODIS observations. *Remote Sens. Environ.* **2020**, *239*, 111628. [CrossRef]
5. Zolkos, S.G.; Goetz, S.J.; Dubayah, R. A meta-analysis of terrestrial aboveground biomass estimation using lidar remote sensing. *Remote Sens. Environ.* **2013**, *128*, 289–298. [CrossRef]
6. Chen, Q.; McRoberts, R.E.; Wang, C.; Radtke, P.J. Forest aboveground biomass mapping and estimation across multiple spatial scales using model-based inference. *Remote Sens. Environ.* **2016**, *184*, 350–360. [CrossRef]
7. Wu, Y.; Ou, G.; Lu, T.; Huang, T.; Zhang, X.; Liu, Z.; Yu, Z.; Guo, B.; Wang, E.; Feng, Z.; et al. Improving Aboveground Biomass Estimation in Lowland Tropical Forests across Aspect and Age Stratification: A Case Study in Xishuangbanna. *Remote Sens.* **2024**, *16*, 1276. [CrossRef]
8. Rasshofer, R.H.; Gresser, K. Automotive radar and lidar systems for next generation driver assistance functions. *Adv. Radio Sci.* **2005**, *3*, 205–209. [CrossRef]
9. Urbazaev, M.; Thiel, C.; Cremer, F.; Dubayah, R.; Migliavacca, M.; Reichstein, M.; Schmullius, C. Estimation of forest aboveground biomass and uncertainties by integration of field measurements, airborne LiDAR, and SAR and optical satellite data in Mexico. *Carbon Balance Manag.* **2018**, *13*, 5. [CrossRef]
10. Khanal, S.; Kc, K.; Fulton, J.P.; Shearer, S.; Ozkan, E. Remote sensing in agriculture—Accomplishments, limitations, and opportunities. *Remote Sens.* **2020**, *12*, 3783. [CrossRef]
11. De Sy, V.; Herold, M.; Achard, F.; Asner, G.P.; Held, A.; Kellndorfer, J.; Verbesselt, J. Synergies of multiple remote sensing data sources for REDD+ monitoring. *Curr. Opin. Environ. Sustain.* **2012**, *4*, 696–706. [CrossRef]
12. Gao, Y.; Lu, D.; Li, G.; Wang, G.; Chen, Q.; Liu, L.; Li, D. Comparative analysis of modeling algorithms for forest aboveground biomass estimation in a subtropical region. *Remote Sens.* **2018**, *10*, 627. [CrossRef]
13. Puliti, S.; Breidenbach, J.; Schumacher, J.; Hauglin, M.; Klingenberg, T.F.; Astrup, R. Above-ground biomass change estimation using national forest inventory data with Sentinel-2 and Landsat. *Remote Sens. Environ.* **2021**, *265*, 112644. [CrossRef]
14. López-Serrano, P.M.; Cárdenas Domínguez, J.L.; Corral-Rivas, J.J.; Jiménez, E.; López-Sánchez, C.A.; Vega-Nieva, D.J. Modeling of aboveground biomass with Landsat 8 OLI and machine learning in temperate forests. *Forests* **2019**, *11*, 11. [CrossRef]
15. Huang, T.; Ou, G.; Wu, Y.; Zhang, X.; Liu, Z.; Xu, H.; Xu, X.; Wang, Z.; Xu, C. Estimating the Aboveground Biomass of Various Forest Types with High Heterogeneity at the Provincial Scale Based on Multi-Source Data. *Remote Sens.* **2023**, *15*, 3550. [CrossRef]
16. Imran, A.; Ahmed, S. Potential of Landsat-8 spectral indices to estimate forest biomass. *Int. J. Hum. Cap. Urban Manag.* **2018**, *3*, 303.
17. Li, C.; Li, Y.; Li, M. Improving forest aboveground biomass (AGB) estimation by incorporating crown density and using landsat 8 OLI images of a subtropical forest in Western Hunan in Central China. *Forests* **2019**, *10*, 104. [CrossRef]
18. Tian, L.; Wu, X.; Tao, Y.; Li, M.; Qian, C.; Liao, L.; Fu, W. Review of remote sensing-based methods for forest aboveground biomass estimation: Progress, challenges, and prospects. *Forests* **2023**, *14*, 1086. [CrossRef]
19. Mutanga, O.; Masenyama, A.; Sibanda, M. Spectral saturation in the remote sensing of high-density vegetation traits: A systematic review of progress, challenges, and prospects. *ISPRS J. Photogramm. Remote Sens.* **2023**, *198*, 297–309. [CrossRef]
20. Zhao, P.; Lu, D.; Wang, G.; Wu, C.; Huang, Y.; Yu, S. Examining spectral reflectance saturation in Landsat imagery and cor-responding solutions to improve forest aboveground biomass estimation. *Remote Sens.* **2016**, *8*, 469. [CrossRef]
21. Ou, G.; Lv, Y.; Xu, H.; Wang, G. Improving forest aboveground biomass estimation of Pinus densata forest in Yunnan of Southwest China by spatial regression using Landsat 8 images. *Remote Sens.* **2019**, *11*, 2750. [CrossRef]
22. Gleason, C.J.; Im, J. A review of remote sensing of forest biomass and biofuel: Options for small-area applications. *GIScience Remote Sens.* **2011**, *48*, 141–170. [CrossRef]

23. Zhang, J.; Zhengjun, L.; Xiaoxia, S. Changing landscape in the Three Gorges Reservoir Area of Yangtze River from 1977 to 2005: Land use/land cover, vegetation cover changes estimated using multi-source satellite data. *Int. J. Appl. Earth Obs. Geoinf.* **2009**, *11*, 403–412. [CrossRef]
24. Steininger, M. Satellite estimation of tropical secondary forest above-ground biomass: Data from Brazil and Bolivia. *Int. J. Remote Sens.* **2000**, *21*, 1139–1157. [CrossRef]
25. Zhu, X.; Liu, D. Improving forest aboveground biomass estimation using seasonal Landsat NDVI time-series. *ISPRS J. Photogramm. Remote Sens.* **2015**, *102*, 222–231. [CrossRef]
26. Chen, Y.; Li, L.; Lu, D.; Li, D. Exploring bamboo forest aboveground biomass estimation using Sentinel-2 data. *Remote Sens.* **2018**, *11*, 7. [CrossRef]
27. Jha, N.; Tripathi, N.K.; Barbier, N.; Virdis, S.G.; Chanthorn, W.; Viennois, G.; Brockelman, W.Y.; Nathalang, A.; Tongsima, S.; Sasaki, N. The real potential of current passive satellite data to map aboveground biomass in tropical forests. *Remote Sens. Ecol. Conserv.* **2021**, *7*, 504–520. [CrossRef]
28. Kasischke, E.S.; Melack, J.M.; Dobson, M.C. The use of imaging radars for ecological applications—A review. *Remote Sens. Environ.* **1997**, *59*, 141–156. [CrossRef]
29. Kaufman, Y.J.; Tanre, D. Strategy for direct and indirect methods for correcting the aerosol effect on remote sensing: From AVHRR to EOS-MODIS. *Remote Sens. Environ.* **1996**, *55*, 65–79. [CrossRef]
30. Kolb, A.; Diekmann, M. Effects of environment, habitat configuration and forest continuity on the distribution of forest plant species. *J. Veg. Sci.* **2004**, *15*, 199–208. [CrossRef]
31. Duivenvoorden, J.E. Tree species composition and rain forest-environment relationships in the middle Caquetá area, Colombia, NW Amazonia. *Vegetatio* **1995**, *120*, 91–113. [CrossRef]
32. Moore, I.D.; Norton, T.; Williams, J.E. Modelling environmental heterogeneity in forested landscapes. *J. Hydrol.* **1993**, *150*, 717–747. [CrossRef]
33. Xia, K.; Daws, M.I.; Peng, L.L. Climate drives patterns of seed traits in Quercus species across China. *New Phytol.* **2022**, *234*, 1629–1638. [CrossRef] [PubMed]
34. Asner, G.P.; Flint Hughes, R.; Varga, T.A.; Knapp, D.E.; Kennedy-Bowdoin, T. Environmental and biotic controls over aboveground biomass throughout a tropical rain forest. *Ecosystems* **2009**, *12*, 261–278. [CrossRef]
35. Theissen, T.; Otte, A.; Waldhardt, R. High-mountain landscape classification to analyze patterns of land use and potential natural vegetation. *Land* **2022**, *11*, 1085. [CrossRef]
36. Lamsal, P.; Kumar, L.; Aryal, A.; Atreya, K. Invasive alien plant species dynamics in the Himalayan region under climate change. *Ambio* **2018**, *47*, 697–710. [CrossRef]
37. Yang, Y.; Tian, K.; Hao, J.; Pei, S.; Yang, Y. Biodiversity and biodiversity conservation in Yunnan, China. *Biodivers. Conserv.* **2004**, *13*, 813–826. [CrossRef]
38. Fan, Z.-X.; Thomas, A. Spatiotemporal variability of reference evapotranspiration and its contributing climatic factors in Yunnan Province, SW China, 1961–2004. *Clim. Chang.* **2013**, *116*, 309–325. [CrossRef]
39. Wu, Z.; Zhu, Y. *The Vegetation of Yunnan*; Science Press: Beijing, China, 1987.
40. Singh, J.; Rawat, Y.; Chaturvedi, O. Replacement of oak forest with pine in the Himalaya affects the nitrogen cycle. *Nature* **1984**, *311*, 54–56. [CrossRef]
41. Xiao, X.; Haberle, S.G.; Shen, J.; Yang, X.; Han, Y.; Zhang, E.; Wang, S. Latest Pleistocene and Holocene vegetation and climate history inferred from an alpine lacustrine record, northwestern Yunnan Province, southwestern China. *Quat. Sci. Rev.* **2014**, *86*, 35–48. [CrossRef]
42. Xu, J.; Jiang, H. *Forests of Yunnan*; Yunnan Science and Technology Press: Kunming, China, 1988.
43. Xu, H.; Zhang, Z.; Ou, G.; Shi, H. *A Study on Estimation and Distribution for Forest Biomass and Carbon Storage in Yunnan Province*; Yunnan Science and Technology Press: Kunming, China, 2019.
44. Liu, J.; Weng, F.; Li, Z.; Cribb, M.C. Hourly PM2. 5 estimates from a geostationary satellite based on an ensemble learning algorithm and their spatiotemporal patterns over central east China. *Remote Sens.* **2019**, *11*, 2120. [CrossRef]
45. Wen, L.; Li, Z. Driving forces of national and regional CO_2 emissions in China combined IPAT-E and PLS-SEM model. *Sci. Total Environ.* **2019**, *690*, 237–247. [CrossRef]
46. Wang, S.; Li, R.; Wu, Y.; Wang, W. Estimation of surface soil moisture by combining a structural equation model and an artificial neural network (SEM-ANN). *Sci. Total Environ.* **2023**, *876*, 162558. [CrossRef] [PubMed]
47. Moradi, F.; Darvishsefat, A.A.; Pourrahmati, M.R.; Deljouei, A.; Borz, S.A. Estimating aboveground biomass in dense Hyrcanian forests by the use of Sentinel-2 data. *Forests* **2022**, *13*, 104. [CrossRef]
48. Celleri, C.; Zapperi, G.; González Trilla, G.; Pratolongo, P. Assessing the capability of broadband indices derived from Landsat 8 Operational Land Imager to monitor above ground biomass and salinity in semiarid saline environments of the Bahía Blanca Estuary, Argentina. *Int. J. Remote Sens.* **2019**, *40*, 4817–4838. [CrossRef]
49. Muñoz-Huerta, R.F.; Guevara-Gonzalez, R.G.; Contreras-Medina, L.M.; Torres-Pacheco, I.; Prado-Olivarez, J.; Ocampo-Velazquez, R.V. A review of methods for sensing the nitrogen status in plants: Advantages, disadvantages and recent advances. *Sensors* **2013**, *13*, 10823–10843. [CrossRef]

50. Wang, J.; Ding, J.; Yu, D.; Ma, X.; Zhang, Z.; Ge, X.; Teng, D.; Li, X.; Liang, J.; Lizaga, I. Capability of Sentinel-2 MSI data for monitoring and mapping of soil salinity in dry and wet seasons in the Ebinur Lake region, Xinjiang, China. *Geoderma* **2019**, *353*, 172–187. [CrossRef]
51. Fu, B.; Liu, S.; Ma, K.; Zhu, Y. Relationships between soil characteristics, topography and plant diversity in a heterogeneous deciduous broad-leaved forest near Beijing, China. *Plant Soil* **2004**, *261*, 47–54. [CrossRef]
52. Glaser, B.; Lehmann, J.; Zech, W. Ameliorating physical and chemical properties of highly weathered soils in the tropics with charcoal—A review. *Biol. Fertil. Soils* **2002**, *35*, 219–230. [CrossRef]
53. Cailleret, M.; Heurich, M.; Bugmann, H. Reduction in browsing intensity may not compensate climate change effects on tree species composition in the Bavarian Forest National Park. *For. Ecol. Manag.* **2014**, *328*, 179–192. [CrossRef]
54. Macek, M.; Kopecký, M.; Wild, J. Maximum air temperature controlled by landscape topography affects plant species composition in temperate forests. *Landsc. Ecol.* **2019**, *34*, 2541–2556. [CrossRef]
55. Schlesinger, W.H.; Dietze, M.C.; Jackson, R.B.; Phillips, R.P.; Rhoades, C.C.; Rustad, L.E.; Vose, J.M. Forest biogeochemistry in response to drought. *Glob. Chang. Biol.* **2016**, *22*, 2318–2328. [CrossRef] [PubMed]
56. Hoylman, Z.H.; Jencso, K.G.; Hu, J.; Holden, Z.A.; Martin, J.T.; Gardner, W.P. The climatic water balance and topography control spatial patterns of atmospheric demand, soil moisture, and shallow subsurface flow. *Water Resour. Res.* **2019**, *55*, 2370–2389. [CrossRef]
57. Thomas, G.; Dalal, R.; Standley, J. No-till effects on organic matter, pH, cation exchange capacity and nutrient distribution in a Luvisol in the semi-arid subtropics. *Soil Tillage Res.* **2007**, *94*, 295–304. [CrossRef]
58. Lützow, M.V.; Kögel-Knabner, I.; Ekschmitt, K.; Matzner, E.; Guggenberger, G.; Marschner, B.; Flessa, H. Stabilization of organic matter in temperate soils: Mechanisms and their relevance under different soil conditions—A review. *Eur. J. Soil Sci.* **2006**, *57*, 426–445. [CrossRef]
59. Ross, D.; Matschonat, G.; Skyllberg, U. Cation exchange in forest soils: The need for a new perspective. *Eur. J. Soil Sci.* **2008**, *59*, 1141–1159. [CrossRef]
60. Sharma, A.; Weindorf, D.C.; Wang, D.; Chakraborty, S. Characterizing soils via portable X-ray fluorescence spectrometer: 4. Cation exchange capacity (CEC). *Geoderma* **2015**, *239*, 130–134. [CrossRef]
61. Smith, P. Soils and climate change. *Curr. Opin. Environ. Sustain.* **2012**, *4*, 539–544. [CrossRef]
62. Certini, G.; Scalenghe, R. The crucial interactions between climate and soil. *Sci. Total Environ.* **2023**, *856*, 159169. [CrossRef]
63. Ravi, S.; Breshears, D.D.; Huxman, T.E.; D'Odorico, P. Land degradation in drylands: Interactions among hydrologic–aeolian erosion and vegetation dynamics. *Geomorphology* **2010**, *116*, 236–245. [CrossRef]
64. Corwin, D.L. Climate change impacts on soil salinity in agricultural areas. *Eur. J. Soil Sci.* **2021**, *72*, 842–862. [CrossRef]
65. Dillon, G.K.; Holden, Z.A.; Morgan, P.; Crimmins, M.A.; Heyerdahl, E.K.; Luce, C.H. Both topography and climate affected forest and woodland burn severity in two regions of the western US, 1984 to 2006. *Ecosphere* **2011**, *2*, 1–33. [CrossRef]
66. Sobek, S.; Tranvik, L.J.; Prairie, Y.T.; Kortelainen, P.; Cole, J.J. Patterns and regulation of dissolved organic carbon: An analysis of 7,500 widely distributed lakes. *Limnol. Oceanogr.* **2007**, *52*, 1208–1219. [CrossRef]
67. Zhou, Y.; Yi, Y.; Liu, H.; Song, J.; Jia, W.; Zhang, S. Altitudinal trends in climate change result in radial growth variation of Pinus yunnanensis at an arid-hot valley of southwest China. *Dendrochronologia* **2022**, *71*, 125914. [CrossRef]
68. Xu, Z.; Zhao, B.; Wang, Y.; Xiao, J.; Wang, X. Composting process and odor emission varied in windrow and trough composting system under different air humidity conditions. *Bioresour. Technol.* **2020**, *297*, 122482. [CrossRef]
69. Keitt, T.H.; Bjørnstad, O.N.; Dixon, P.M.; Citron-Pousty, S. Accounting for spatial pattern when modeling organism-environment interactions. *Ecography* **2002**, *25*, 616–625. [CrossRef]
70. Trenberth, K.E. Changes in precipitation with climate change. *Clim. Res.* **2011**, *47*, 123–138. [CrossRef]
71. Moser, G.; Leuschner, C.; Hertel, D.; Graefe, S.; Soethe, N.; Iost, S. Elevation effects on the carbon budget of tropical mountain forests (S Ecuador): The role of the belowground compartment. *Glob. Chang. Biol.* **2011**, *17*, 2211–2226. [CrossRef]
72. Körner, C. The use of 'altitude'in ecological research. *Trends Ecol. Evol.* **2007**, *22*, 569–574. [CrossRef]
73. Obanor, F.O.; Walter, M.; Jones, E.E.; Jaspers, M.V. Effect of temperature, relative humidity, leaf wetness and leaf age on Spilocaea oleagina conidium germination on olive leaves. *Eur. J. Plant Pathol.* **2008**, *120*, 211–222. [CrossRef]
74. Sheil, D.; Murdiyarso, D. How forests attract rain: An examination of a new hypothesis. *Bioscience* **2009**, *59*, 341–347. [CrossRef]
75. Price, K. Effects of watershed topography, soils, land use, and climate on baseflow hydrology in humid regions: A review. *Prog. Phys. Geogr.* **2011**, *35*, 465–492. [CrossRef]
76. Unger, M.; Homeier, J.; Leuschner, C. Effects of soil chemistry on tropical forest biomass and productivity at different elevations in the equatorial Andes. *Oecologia* **2012**, *170*, 263–274. [CrossRef]
77. Knipling, E.B. Physical and physiological basis for the reflectance of visible and near-infrared radiation from vegetation. *Remote Sens. Environ.* **1970**, *1*, 155–159. [CrossRef]
78. Gilgen, A.K.; Buchmann, N. Response of temperate grasslands at different altitudes to simulated summer drought differed but scaled with annual precipitation. *Biogeosciences* **2009**, *6*, 2525–2539. [CrossRef]
79. Chen, F.; Fan, Z.; Niu, S.; Zheng, J. The influence of precipitation and consecutive dry days on burned areas in Yunnan Province, Southwestern China. *Adv. Meteorol.* **2014**, *2014*, 748923. [CrossRef]

80. Hernández-Stefanoni, J.L.; Castillo-Santiago, M.Á.; Mas, J.F.; Wheeler, C.E.; Andres-Mauricio, J.; Tun-Dzul, F.; George-Chacón, S.P.; Reyes-Palomeque, G.; Castellanos-Basto, B.; Vaca, R. Improving aboveground biomass maps of tropical dry forests by integrating LiDAR, ALOS PALSAR, climate and field data. *Carbon Balance Manag.* **2020**, *15*, 15. [CrossRef]
81. Fu, L.; Lei, X.; Hu, Z.; Zeng, W.; Tang, S.; Marshall, P.; Cao, L.; Song, X.; Yu, L.; Liang, J. Integrating regional climate change into allometric equations for estimating tree aboveground biomass of Masson pine in China. *Ann. For. Sci.* **2017**, *74*, 42. [CrossRef]
82. Shao, G.; Shao, G.; Gallion, J.; Saunders, M.R.; Frankenberger, J.R.; Fei, S. Improving Lidar-based aboveground biomass estimation of temperate hardwood forests with varying site productivity. *Remote Sens. Environ.* **2018**, *204*, 872–882. [CrossRef]
83. Zhou, J.-J.; Zhao, Z.; Zhao, Q.; Zhao, J.; Wang, H. Quantification of aboveground forest biomass using Quickbird imagery, topographic variables, and field data. *J. Appl. Remote Sens.* **2013**, *7*, 073484. [CrossRef]
84. Su, Y.; Guo, Q.; Xue, B.; Hu, T.; Alvarez, O.; Tao, S.; Fang, J. Spatial distribution of forest aboveground biomass in China: Estimation through combination of spaceborne lidar, optical imagery, and forest inventory data. *Remote Sen. Environ.* **2016**, *173*, 187–199. [CrossRef]